JGR Solid Earth

RESEARCH ARTICLE
10.1029/2022JB025069

Microscale Spatial Variations in Coseismic Temperature Rise on Hematite Fault Mirrors in the Wasatch Fault Damage Zone

Robert G. McDermott[1,2], Alexis K. Ault[2], Kelsey F. Wetzel[2], James P. Evans[2], and Fen-Ann Shen[3]

[1]U.S. Geological Survey, Alaska Science Center, Anchorage, AK, USA, [2]Department of Geosciences, Utah State University, Logan, UT, USA, [3]Microscopy Core Facility, Utah State University, Logan, UT, USA

Key Points:

- Microscopy and electron backscatter diffraction reveal microscale variations in microstructures on Wasatch hematite fault mirrors
- Coseismic temperatures and deformation mechanisms vary with shear zone thickness and fault surface roughness
- Wasatch damage zone hematite fault mirrors accommodated small earthquakes

Supporting Information:

Supporting Information may be found in the online version of this article.

Correspondence to:

R. G. McDermott,
rmcdermott@usgs.gov

Citation:

McDermott, R. G., Ault, A. K., Wetzel, K. F., Evans, J. P., & Shen, F.-A. (2023). Microscale spatial variations in coseismic temperature rise on hematite fault mirrors in the Wasatch fault damage zone. *Journal of Geophysical Research: Solid Earth*, *128*, e2022JB025069. https://doi.org/10.1029/2022JB025069

Received 27 JUN 2022
Accepted 10 MAR 2023

Author Contributions:

Conceptualization: Robert G. McDermott, Alexis K. Ault, James P. Evans
Formal analysis: Robert G. McDermott, Alexis K. Ault, Kelsey F. Wetzel
Investigation: Robert G. McDermott, Alexis K. Ault, Kelsey F. Wetzel, James P. Evans, Fen-Ann Shen
Resources: Robert G. McDermott, Alexis K. Ault
Supervision: Alexis K. Ault

Abstract Coseismic temperature rise activates fault dynamic weakening that promotes earthquake rupture propagation. The spatial scales over which peak temperatures vary on slip surfaces are challenging to identify in the rock record. We present microstructural observations and electron backscatter diffraction data from three small-displacement hematite-coated fault mirrors (FMs) in the Wasatch fault damage zone, Utah, to evaluate relations between fault properties, strain localization, temperature rise, and weakening mechanisms during FM development. Millimeter- to cm-thick, matrix-supported, hematite-cemented breccia is cut by ~25–200 μm-thick, texturally heterogeneous veins that form the hematite FM volume (FMV). Grain morphologies and textures vary with FMV thickness over μm to mm lengthscales. Cataclasite grades to ultracataclasite where FMV thickness is greatest. Thinner FMVs and geometric asperities are characterized by particles with subgrains, serrated grain boundaries, and(or) low-strain polygonal grains that increase in size with proximity to the FM surface. Comparison to prior hematite deformation experiments suggests FM temperatures broadly range from ≥400°C to ≥800–1100°C, compatible with observed coeval brittle and plastic deformation mechanisms, over sub-mm scales on individual slip surfaces during seismic slip. We present a model of FM development by episodic hematite precipitation, fault reactivation, and strain localization, where the thickness of hematite veins controls the width of the deforming zones during subsequent fault slip, facilitating temperature rise and thermally activated weakening. Our data document intrasample coseismic temperatures, resultant deformation and dynamic weakening mechanisms, and the length scales over which these vary on slip surfaces.

Plain Language Summary Earthquakes produce friction-generated heat pulses that in turn influence their mechanics. Fault surfaces produced or modified by past earthquakes may carry a signature of this heat and are geological archives of the mechanisms that facilitate earthquake-producing slip. Identifying and interpreting earthquake-related thermal signatures, how and why they may vary on a fault surface, and their mechanical influence on earthquakes is challenging. We characterize three, thin, small hematite-coated fault surfaces from the Wasatch fault in northern Utah with microscopy techniques that illuminate hematite structure and the physical mechanisms of deformation at micro- to nano-scale. Microstructures diagnostic of transient, hot temperatures vary on a single fault surface over sub-mm scales and are linked to multiple hypothesized deformation mechanisms that facilitate earthquake slip. Fault properties such as thickness of the deforming zone and surface roughness influence variable temperature rise. Our results provide insight into how temperatures and the physical mechanisms that facilitate earthquakes vary on a single fault surface, and the factors and geological history that promote these variations.

1. Introduction

Dynamic strength changes on a slipping fault surface are a key component of the propagation and arrest of earthquake ruptures (Dieterich, 1992; Scholz, 1998). Many of these changes are promoted by thermally activated dynamic weakening mechanisms (e.g., Di Toro et al., 2011; Pozzi et al., 2021). Rotary shear experiments and field studies of exhumed fault rocks document a myriad of dynamic weakening mechanisms, including flash heating and failure at geometric asperities (Goldsby & Tullis, 2011; Kohli et al., 2011; Rice, 2006), melting of rock and lubrication (Di Toro et al., 2006; Spray, 2005; Ujiie et al., 2007), thermal pressurization and fluidization (Ujiie et al., 2011; Wibberley & Shimamoto, 2005), gel formation (Faber et al., 2014; Kirkpatrick et al., 2013; Rowe et al., 2019), and nanoparticle lubrication by comminution and phase changes (Han et al., 2011; Verberne et al., 2014). Coseismic temperature rise, despite its short duration (on the scale of seconds), may be

Writing – original draft: Robert G. McDermott, Alexis K. Ault, James P. Evans
Writing – review & editing: Robert G. McDermott, Alexis K. Ault, James P. Evans

sufficient to trigger local crystal plasticity, even in the brittle crust (De Paola et al., 2015; Ohl et al., 2021; Pozzi et al., 2019, 2021). Different dynamic weakening mechanisms are active at variable threshold temperatures, and thus the distribution of heat across a fault surface directly impacts earthquake mechanics (e.g., Di Toro et al., 2011; Kirkpatrick & Shipton, 2009; Spagnuolo et al., 2016). Identifying these mechanisms in space and time and characterizing the interplay between brittle and plastic deformation in the nominally brittle regime informs in situ earthquake physics.

Coseismic temperature rise depends on a variety of factors including ambient temperature, stress, displacement, slip velocity, and the intrinsic properties (frictional strength, thermal properties, thickness, surface roughness) of a deforming zone that evolve in space and time (Cardwell et al., 1978; Lachenbruch, 1986; Platt et al., 2014; Rice, 2006). Lithologies incorporated into a fault zone and hydrothermal alteration impart mechanical heterogeneity (Bruhn et al., 1994; Chester et al., 1993; Goddard & Evans, 1995; Williams et al., 2021). The thickness of the slipping zone that accommodates the bulk of deformation may vary from microns to meters within a single fault strand (Chester & Logan, 1986; Faulkner et al., 2003; Kirkpatrick et al., 2018). Slip localization and narrower deforming zones promote higher coseismic temperatures and dynamic weakening during repeated activation of slip surfaces and/or over the course of a single slip event (Shervais & Kirkpatrick, 2016; Smith et al., 2015). Prior work on natural faults suggests the potential for large coseismic temperature and(or) dynamic strength variations related to shear zone thickness (Armstrong et al., 2022; Coffey et al., 2019; Kirkpatrick & Shipton, 2009; Odlum et al., 2022; Savage & Polissar, 2019). Fault roughness also evolves with slip and controls spatially variable coseismic temperature rise via locally concentrated shear stress at geometric asperities (Aretusini et al., 2021; Rice, 2006; Sagy et al., 2007).

Documentation of fault surface paleotemperatures and associated deformation and weakening mechanisms from exhumed fault rocks anchors our understanding of the relation between fault evolution and seismogenesis. Hematite-coated fault surfaces are amenable to integrated microstructural and thermochronometry analysis that can characterize the timing and conditions of mineralization during fault slip, slip rates and temperatures, and/or the post-formation thermal and mechanical history (Ault, 2020; McDermott et al., 2017, 2021). Rotary shear experiments show hematite is frictionally weak and exhibits subtle dynamic weakening behavior (Calzolari et al., 2020). The Brigham City segment of the Wasatch fault zone (WFZ) in northeastern, UT, USA, hosts abundant, mirrored, minor hematite-coated discrete fault surfaces (fault mirrors, or FMs) that accommodated past nano-to microseismicity (M_w −3 to 0; cf. Ault et al., 2015; Eaton et al., 2016; Evans et al., 2014; McDermott et al., 2017). Prior work utilized hematite (U-Th)/He thermochronometry and microstructural analysis as a paleothermometer to reveal highly localized temperatures >1200°C potentially due to asperity flash heating during coseismic slip on a suite of hematite FMs (Ault et al., 2015; McDermott et al., 2017). However, the prevalence of asperity flash heating or other dynamic weakening mechanisms on individual FMs as they develop is not known.

We investigate three WFZ FMs that are representative of FMs exposed throughout the broader study area (Evans & Langrock, 1994; McDermott et al., 2017) with field to nanoscale observations from scanning electron microscopy (SEM) and electron backscatter diffraction (EBSD). Variation of microstructures and inferred deformation mechanisms both across and perpendicular to the FM surfaces reflect spatially variable coseismic temperature rise linked to fault properties (e.g., thickness of the deforming zone and fault surface roughness). Field and microstructural observations support multiple small-magnitude hydrothermal and fault reactivation events on individual surfaces at shallow crustal depths. We document the spatial scales of multiple temperature-sensitive dynamic weakening mechanisms operative between FMs and across slip surfaces during individual events and develop a conceptual model for FM evolution.

2. Wasatch Fault Zone and Hematite Fault Mirrors

The WFZ is a ~370 km long, seismogenic, and segmented normal fault that demarcates the easternmost extent of Miocene-present Basin and Range extension in northeastern Utah (Figure 1a; Machette et al., 1991). In the study area at the southern end of the Brigham City segment of the WFZ, the fault zone cuts Paleoproterozoic hornblende- and biotite-bearing quartz monzonite gneiss, amphibolite, and granitic pegmatite, with younger sedimentary rocks in the hanging wall (Figure 1b; Bryant, 1988; Crittenden & Sorensen, 1985; Evans & Langrock, 1994). The Farmington Canyon Complex in our study area is overlain by Cambrian sedimentary rocks of the Brigham Group, upon which the Neoproterozoic Facer Formation and (informally defined) formation of Perry Canyon are emplaced by the Willard thrust (Figure 1b; Crittenden & Sorensen, 1985; Yonkee et al., 2019). Sevier

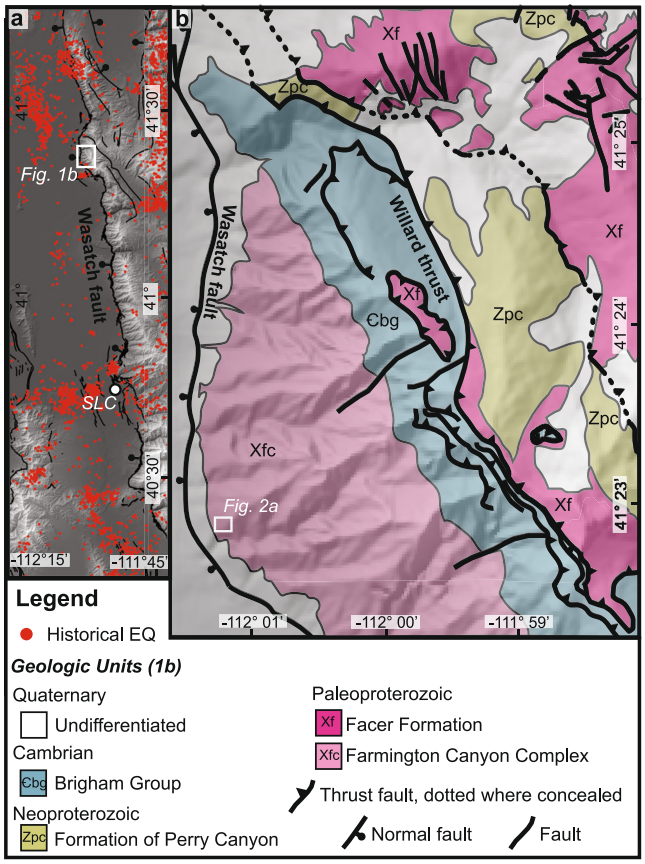

Figure 1. Wasatch fault zone (WFZ) and regional geology. (a) Hillshade of the Wasatch Front with Quaternary trace of the Wasatch fault (from Utah Geological Survey Quaternary Fault and Fold Database) and historical seismicity (red dots; Arabasz et al., 2017). (b) Bedrock geology of study area along the Brigham City segment of the WFZ. Geology after Crittenden and Sorensen (1985). Legend applies to (a) and (b). EQ-earthquake, SLC-Salt Lake City.

orogeny thrusting occurred ~130–90 Ma (Yonkee et al., 2019). Deformation in the WFZ began ~18–12 Ma (Ehlers et al., 2003; Parry & Bruhn, 1987) and continues to the present (Figure 1a). Full- and partial-segment-rupturing ~ M_w 7 earthquakes are documented every ~1,060–1,500 yr during the Holocene (DuRoss et al., 2016).

The active trace of the WFZ is expressed within Quaternary sediments (Figure 1b), but a ~300–400 m-wide fault damage zone crops out within the footwall of the southern Brigham City segment. This damage zone hosts chlorite breccia and phyllonite, rare gouge, Fe-oxide rich cataclasite a few to tens of millimeters in thickness, disseminated Fe-oxide alteration, abundant ~mm-thick specular hematite (specularite) veins and FMs (Evans & Langrock, 1994), and silica-rich FMs (Houser et al., 2021). Hematite FMs and veins are observed as principally distributed in the damage zones of mesoscale normal faults subsidiary to the trace of the active WFZ (McDermott et al., 2017). Prior field study reveals hematite FMs are often localized within mm- to cm-thick hematite-cemented breccia or specular hematite (specularite) veins (Ault et al., 2015; Evans & Langrock, 1994; McDermott et al., 2017). FM striae have diverse orientation and kinematics, but show dominantly down-to-the-west normal slip, consistent with Basin and Range extension accommodated along the WFZ (Evans & Langrock, 1994).

Previous geochemical, textural, and thermochronometric analyses suggest some FMs accommodated seismic slip and transient elevated temperatures facilitated by asperity flash-heating. Localized, coseismic temperature rise is supported by (a) the presence of surficial Fe^{2+}, indicative of high-temperature Fe reduction; (b) polygonal (i.e., triple-junction forming); and(or) grains with lobate grain boundaries directly at the FM, suggestive of high-temperature sintering and(or) annealing; and (c) hematite (U-Th)/He data from FMs, which show spatially variable thermal resetting of the (U-Th)/He system (i.e., He loss), in regions characterized by high-temperatures microstructures (Ault et al., 2015; Evans et al., 2014; McDermott et al., 2017). Patterns of He loss require local coseismic temperatures >1200°C (McDermott et al., 2017). Comparison of apatite and hematite (U-Th)/He data constrain the timing and depth of these past small-magnitude earthquakes to ≤4.5 Ma and ≤2 km (assuming a 25–30°C/km geothermal gradient; Ault et al., 2015; McDermott et al., 2017). Hematite (U-Th)/He dates from undeformed specularite veins material underlying FMs range from ~12 to ~110 Ma, implying at least some hematite alteration precedes Miocene deformation in the WFZ (McDermott et al., 2017).

3. Field Observations and Fault Mirror Samples

We build on prior work and report new field observations, geological mapping (~1:200 scale), and structural measurements from a suite of outcrops containing abundant hematite FMs located ~280 m east from the Quaternary trace of the WFZ. Mesoscale (ten to tens of meters in trace length) subsidiary faults in the WFZ cut foliated quartz monzonite gneiss and amphibolite (Figures 2a and 2b). At our Pearsons Canyon study locale, an SW-striking normal fault zone is characterized by highly fractured bedrock flanked by planar slip surfaces that are decorated with ~1–4 m^2 patches of weathered hematite (Figure 2c). Other N-trending normal fault traces are expressed geomorphically as small gullies across which amphibolite layers are offset with a vertical separation of ~20 m.

Abundant hematite FMs sporadically decorate the damage zones of SW- and N- trending mesoscale faults (Figures 2c and 2d), with local structural intensity as high as ~20 discrete FMs/m (Figure 2d). The size of FMs (either trace lengths in cross-section or the longest dimension of exposed patches) ranges from tens of centimeters to sub-meters (Figures 2c–2f). Some FMs are underlain by, and subparallel to, hematite-cemented breccia and hematite veins that cross-cut crystalline basement (Figure 2e). FMs have striae (rectilinear grooves, wear tracks, and tool marks) indicative of both oblique normal and reverse slip (Figures 2b and 2f). Displacement markers across FMs were not observed in this outcrop, although a site ~100 m to the west contains FMs that cut gneiss

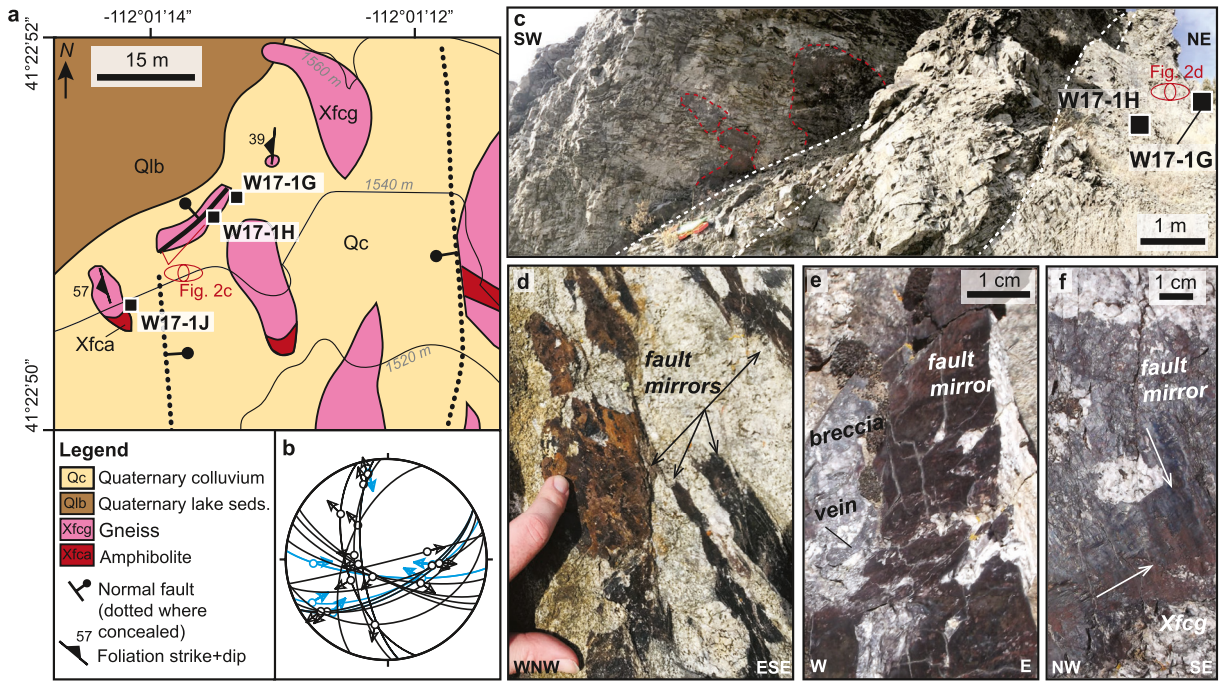

Figure 2. Field setting of Wasatch fault zone hematite fault mirrors (FMs). (a) 1:200-scale geologic map of study area with sample locales (black boxes). (b) Equal-area plot of hematite FM orientations (black, blue great circles indicate normal-, reverse-sense faults) and striae orientations (white circles, arrows denote hanging wall slip sense). (c) Field photograph (looking NNE) of mesoscale E-W trending normal fault. Fault is marked by irregular patches of ruddy hematite (dashed red outlines) and pulverized rock. Locations of FM samples W17-1G and W17-1H indicated by black boxes. (d) Field photo (looking NNE) of multiple subparallel hematite FMs (black arrows). Location denoted on (c). (e) Field photo of hematite FM W17-1G showing underlying hematite-cemented breccia and cross-cutting hematite vein (looking N). (f) Field photo of multiply striated FM (looking NE). White arrows denote striae orientation and movement of missing block determined from tool marks.

bands and specularite veins with ~<1–2 cm of separation (Figure S1 in Supporting Information S1). FM surfaces are commonly multiply striated (Figure 2f), implying these are maximum single-event estimates.

We focus on three samples that preserve unweathered hematite FMs and underlying breccia: W17-1G, W17-1J, and W17-1H (Figure 3). Samples W17-1G and W17-1H are E-striking, steeply S-dipping faults, exhibit striae with normal sense slip, and were collected within 3–4 m of the larger SW-striking normal fault (Figures 2a, 2c, 3a, and 3h). Sample W17-1J was collected from within 3 m of an N-striking normal fault, is subparallel to this structure, and exhibits a single striae set compatible with normal slip (Figures 2a and 3d).

4. Analytical Methods

4.1. Microscopy

We prepared aliquots for microstructural analysis by creating epoxy mounts of each FM sample. Samples were cut perpendicular to the FM surface and oriented with the dominant striae direction parallel to mount surface. Mounts were imaged in reflected light and with SEM. We additionally mounted unpolished FM chips on double-sided copper adhesive tape for map and oblique perspectives and created thin sections of samples W17-1G and W17-1J to aid in microstructural characterization (Figures 3c and 3g). SEM was conducted at the Utah State University Microscopy Core Facility using an FEI Quanta FEG 650 field emission SEM in high-vacuum mode. We imaged samples with secondary electron and backscatter electron detectors to highlight both morphologic and compositional variations, respectively. Carbon-coated mounts and copper adhesive mounts were analyzed under high vacuum at pressures of $<5 \times 10^{-6}$ torr and in low vacuum mode at pressures of 0.08–0.53 torr, respectively. We used an accelerating voltage of 15–20 kV and ~10 mm working distance for all mounts.

4.2. Electron Backscatter Diffraction

Epoxied mounts previously analyzed by SEM were repolished at 1 μm grit to remove carbon-coating and subsequently polished under colloidal silica suspension with a VibroMet 2 vibratory polisher. Hematite, quartz, and

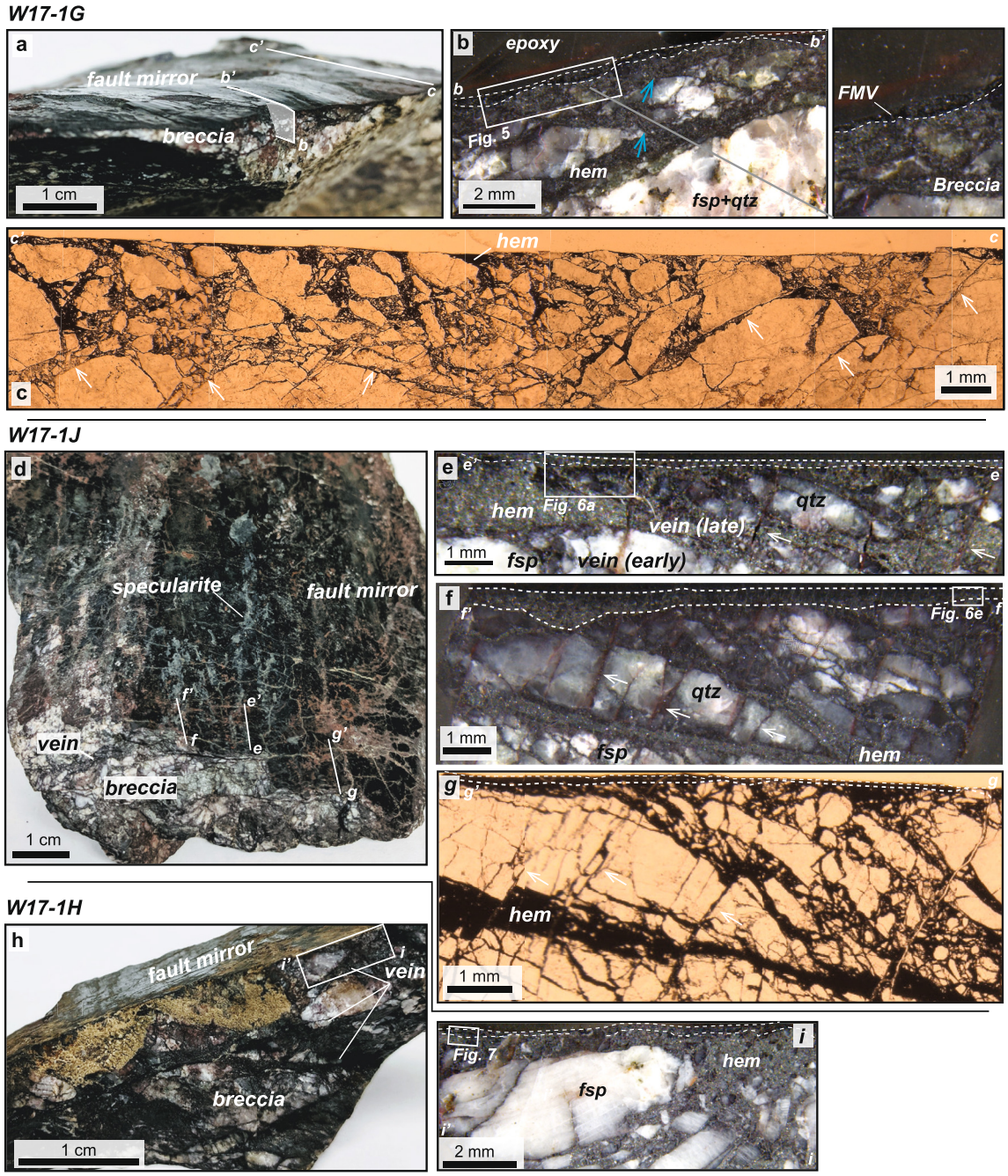

Figure 3. Hematite FM samples. (a) Hand sample photograph of W17-1G. Cut lines for epoxied mount (b–b') and thin section (c–c') denoted. (b) Epoxied mount of W17-1G. Blue arrows point to interpreted Riedel-type shears. White box shows area of microstructural observations in Figure 4. Inset shows detail of breccia and fault mirror volume (FMV) contact (white, dashed). (c) Plane polarized light (PPL) photomicrograph of W17-1G thin section. Jigsaw clast geometry example shown (white, dashed). White arrows point to secondary shear fractures. (d) Hand sample photo of W17-1J and corresponding (e) first epoxied mount, (f) second epoxied mount, and (g) thin section PPL photomicrographs. (h) W17-1H hand sample photograph. (i) W17-1H epoxied mount photomicrograph. See white box in (h) for sample area. Annotations in (d–i) as in (a–c). hem-hematite, qtz-quartz, fsp-feldspar.

feldspar crystal orientation data were collected at 70° sample tilt with an Oxford NordlysMax detector and using the Inorganic Crystal Structure Database. Data were acquired at low-vacuum (typically ~0.05 Torr) conditions with 20 kV accelerating voltage and at a ~3.1 Hz collection rate. Owing to the delicate nature of our samples and large grain size variation between analyzed areas, it was challenging to maintain consistent map areas. Analyzed areas nearest the FM surface range from 375 to 600 μm^2 and data were collected with a 0.1 μm step size. Data

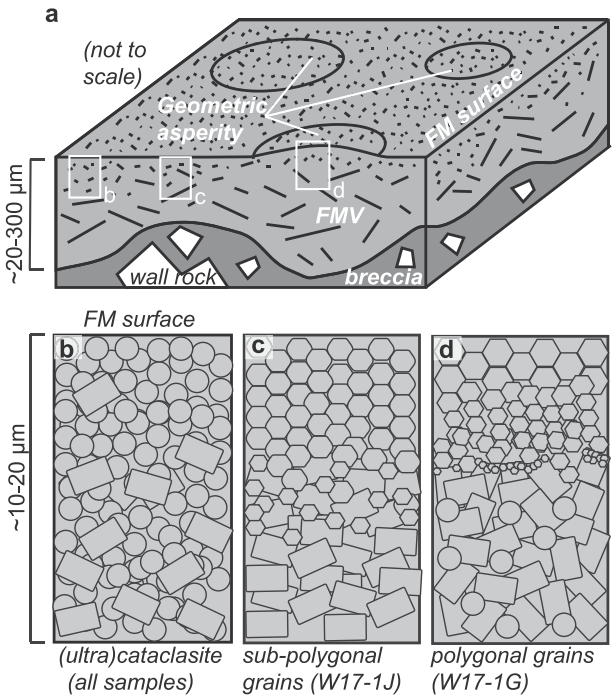

Figure 4. Schematic of hematite microstructure on generic FM. (a) Hematite FM with underlying hematite-cemented breccia and FMV of variable thickness. (b–d) Key microstructures at and ~20 µm below the FM surface. Hematite FMs are characterized by ultracataclasite where the FMV is thick (b), sub-polygonal (including as mantles on plates) where the FMV is thinner (c), and by < 10 µm thick layers of polygonal grains at topographic highs (geometric asperities, (d)).

collected from coarser-grained and more heterogenous areas below the FM surface ranged in area from ~400 to 2,800 µm^2 and were collected with a 0.5 µm step size.

The EBSD data were post-processed with AztecCrystal software following practices outlined in Prior et al. (2009). We applied automatic noise reduction algorithms to target and remove mis-indexed pixels (i.e., large phase or orientation outliers of ≤4 pixels) and zero solution pixels. Subgrain and grain boundaries are delineated by misorientations (i.e., the difference in orientation between two adjacent crystallites) of ≥2° and ≥10°, respectively. We discarded grains comprising <10 pixels, and adjacent grains with 85° ± 5° misorientation about the 02–21 plane were combined into single grains as these likely represent rhombohedral twinning (Ávila et al., 2015). Results are reported as band contrast (related to indexing quality) overlain by inverse pole figure orientations in the sample *x*-direction (IPFx, where *x* is parallel to slip) and (sub)grain boundary maps. Pole figures were generated with one-point-per-grain and presented as upper-hemisphere stereographic projections. Contouring on all pole figures uses a 15° half-width to account for low grain counts (<100) for some map areas. To explore intracrystalline deformation, we conducted misorientation analyses. These results are presented as maps where each pixel is colored by its orientation deviation from the grain average (mis2mean), histograms of misorientation angles for both neighboring and randomly selected pixels (n = 10,000), and inverse misorientation pole figures (MIPFs). The latter shows the orientation of misorientation axes in *crystal* coordinates and thus show if misorientations consistently occur about specific crystallographic axes, often related to intracrystalline slip systems activated during plastic deformation (e.g., Lloyd et al., 1997).

5. Results

We observe two distinct microstructural domains in each sample, visible in hand sample and transmitted light photomicrographs of epoxy mounts, which we term *hematite-cemented breccia* and *fault mirror volume* (FMV; e.g., Figures 3b and 4a). The FMV refers to a layer of deformed hematite, poor in wall-rock clasts, that crosscuts and postdates the underlying hematite-cemented breccia (Figure 3b, inset; cf. Ault et al., 2019). We refer to the uppermost, 2-dimensional surface of the upper FMV as the *FM surface*.

5.1. Hematite Microstructures

5.1.1. Hematite-Cemented Breccia

The hematite-cemented breccia in our studied samples is ~2 mm to >1 cm thick and is generally matrix-supported (Figures 3a, 3d, and 3h). Angular clasts of quartz and feldspar derived from underlying gneiss are hundreds of micrometers to millimeters in their longest dimension (Figures 3c and 3g). Two-dimensional clast percentages vary within and between samples, with ~10%–50% in W17-1G (Figure 3c), ~10%–90% in W17-1J (Figures 3e–3g), and ~60% in W17-1H (Figure 3i). Clasts exhibit jigsaw geometry, defined here as neighboring clasts that can be visually restored with little rotation, and apparent shape-preferred orientation (SPO) imparted by matrix-forming hematite veins oriented ~30–45° to the FM surface (Figures 3c, 3g, and 3i). Matrix hematite consists of little-deformed, ~1–5 µm-thick by ~5 to ≥10 µm-long hematite plates (Figure 5 and Figure S2 in Supporting Information S1).

We observe evidence for multiple generations of hematite-cemented breccia and(or) veins in each sample. Hematite-cemented breccia in W17-1G exhibits clasts of an earlier breccia (Figure 5a). Sample W17-1J hosts clast-supported breccia veins cut by later matrix-supported breccia (Figure 3e). In outcrop and hand sample, hematite-cemented breccias in all samples are cut by later hematite veins that are broadly (sub)parallel to the

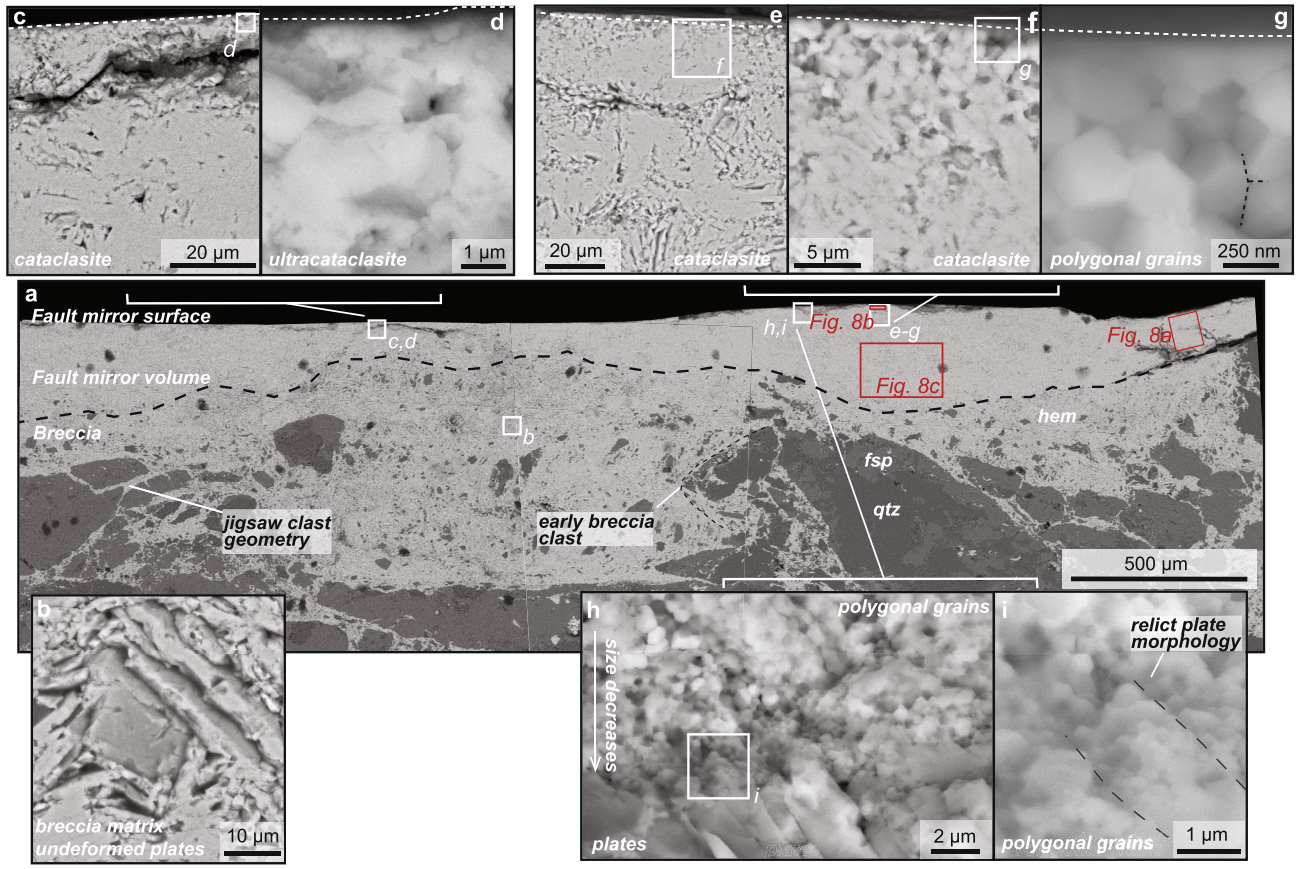

Figure 5. Sample W17-1G microstructures. (a) Backscatter electron (BSE) image; bright hues are hematite, darker grays are feldspar and quartz from gneissic host rock. Black dashed line marks hematite-cemented breccia and FMV boundary. Red boxes show electron backscatter diffraction (EBSD) map areas (Figure 8). (b) Detail of breccia hematite matrix. (c, d) BSE images at increasing magnification (left to right) of hematite cataclasite and ultracataclasite. (e–g) BSE images at increasing magnification of polygonal, triple junction-forming (highlighted with black, dashed lines in (g) hematite grains. (h, i) BSE images taken at increasing magnification of polygonal hematite grains with grain size gradient and overprinting underlying hematite plates. Former plate boundary outlined (black, dashed line) in (j). White-dashed lines in (c–g) denote FM surface.

FM surface (Figures 2e, 3a, 3d, and, 3h). In W17-1G, hematite-cemented breccia is cut and offset by Riedel-type shears emanating from the FMV (Figure 3b).

5.1.2. Fault Mirror Volume

Microstructures and hematite grain size and morphologies of the FMV differ between and within all three samples. These attributes vary across a single FM surface and generally correlate with total FMV thickness and topographic heterogeneity on the FM surface. Below, we describe FMV microstructure for each sample separately, with specific detail given where structure varies with properties of the FMV and FM surface. Relations between hematite microstructure, FMV thickness, and FM surface topography observed across our sample set are shown schematically for a generic FM in Figure 4.

The FMV of W17-1G is nearly pure hematite, ranges from ~80 to ~280 μm thick, and has an undulating but sharp boundary with underlying breccia (Figure 5a). Much of the FMV is hematite cataclasite and protocataclasite (*sensu* Sibson, 1977), with hematite plates that are ~1 μm thick and a few μm to ≥10 μm in length (Figures 5c and 5e). Plate length (and aspect ratio) generally decreases, and the proportion of sub-μm grains increases, toward the FM surface (Figures 5c–5f). Where the FM is planar and the total FMV is ~80 μm thick, the ~10–20 μm directly beneath the FM surface exhibits hematite ultracataclasite with abundant low aspect-ratio nanoparticles (defined as grains with diameter <1 μm; Figures 5c and 5d). In contrast, a ~5–10 μm-thick zone of triple-junction-forming, polygonal hematite grains is the dominant microstructure at an ~1 mm-long topographic high along the FM surface (Figures 5e–5j). Zones of polygonal grains exhibit no SPO and low porosity relative to underlying cataclasite (Figures 5e–5j). Polygonal grain diameter decreases from ~2 to 3 μm at the FM surface

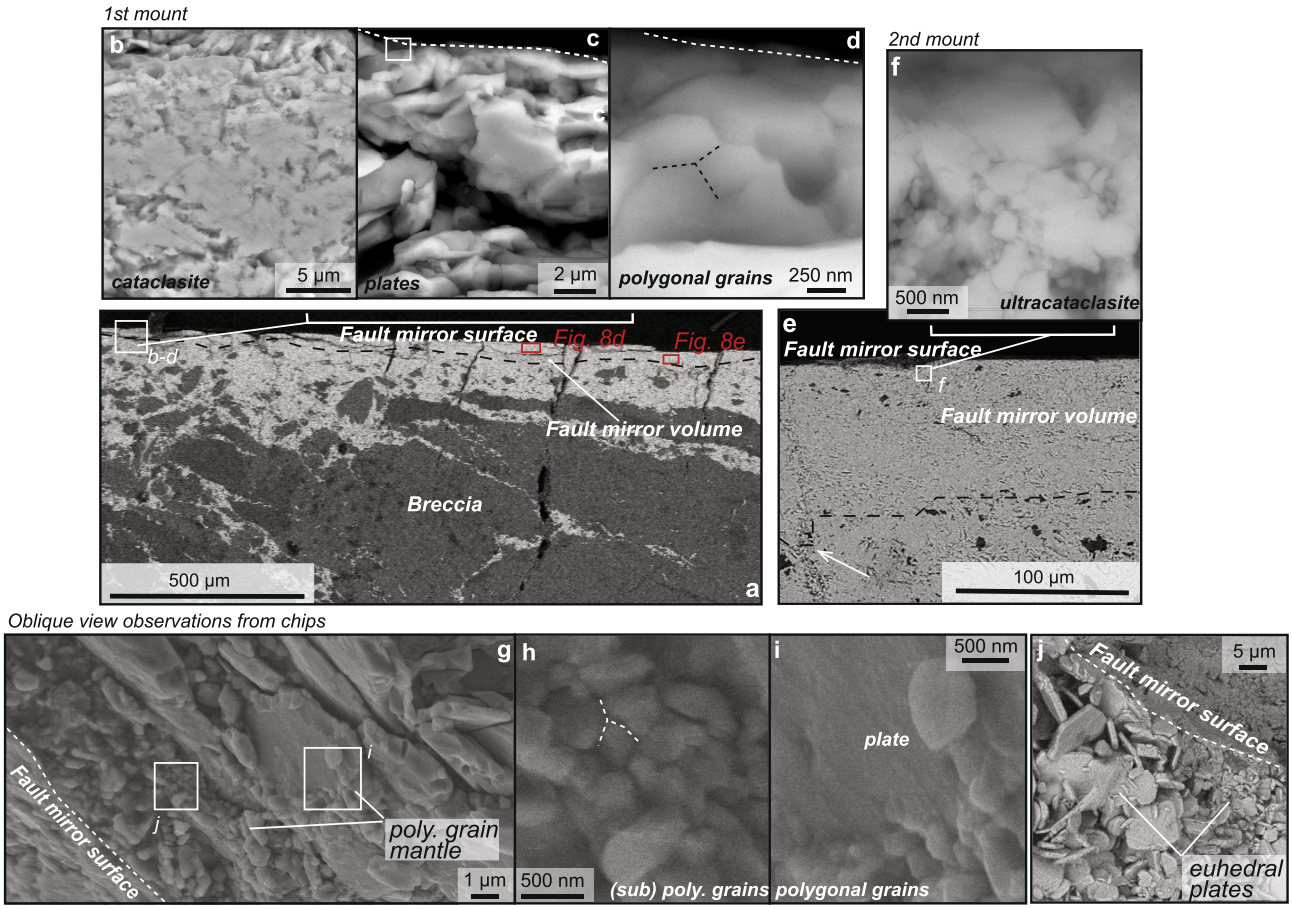

Figure 6. Sample W17-1J microstructures. (a) BSE image of hematite-cemented breccia and FMV (see Figure 3e). Red boxes show EBSD map areas (Figure 8). (b–d) BSE images at increasing magnification (left to right) of hematite cataclasite, plates and polygonal grains. Black dashed lines outline triple junction in (d). (e) BSE image of breccia and FMV from 2nd epoxied mount (see Figure 3f). (f) Ultracataclasite from 2nd epoxied mount. (g) Secondary electron (SE) image from unpolished sample chips (oblique view) of uppermost FMV and FM surface, showing detail of hematite plates with polygonal grain mantles and hematite nanoparticles. (h) SE image showing detail of nanoparticles in (g). White dashed lines outline triple junction. (i) SE image showing detail of plates with polygonal grain mantles in (g). (j) BSE image from additional sample chip with undeformed, euhedral hematite plates. Symbology and annotations in all panels as in Figure 5.

to ≤200 nm, up to 20 μm perpendicular to the FM surface (Figures 5g–5i). Locally, polygonal grains become increasingly sparse with increasing FM-perpendicular distance and are intermingled with cataclastic grains (Figure 5f). Plate tips from underlying hematite intrude at high-angle into zones of polygonal hematite. The tips of these grains have been transformed into polygonal grains, but the morphology of original plate boundaries is preserved (Figures 5h and 5i).

In W17-1J, FMV thickness ranges from ~20–60 μm (Figure 6a) to ~80–100 μm (Figure 6e) in two mounts prepared from material ~1 cm apart (Figure 3d). High-angle secondary shear fractures similar to those in breccia (e.g., Figure 3g) locally offset the FMV (Figure 6e). FMV hematite exhibits cataclastic textures and moderate SPO, with both high and low aspect ratio hematite grains ~1–2 μm in diameter/thickness (Figure 6b). Where the FMV is thinnest, the ~10 μm immediately below the FM surface comprises intermingled sub-μm plates with strong SPO and cataclasite, with the former showing development of <500 nm diameter, triple-junction-forming, polygonal grains at the FM surface (Figures 6c and 6d). Ultracataclasite composed of equant nanoparticles is dominant where the FMV is >80 μm thick (Figures 6e and 6f). In unpolished chips isolated from the FM surface from this sample, we observe a ~5 μm-thick, low-porosity layer of (sub) polygonal grains (Figures 6g and 6h) and intermingled sub-μm-thick plates mantled by smaller polygonal grains (Figure 6i). Elsewhere, pristine, euhedral, ~0.5 μm-thick by ≥ 5 μm-long, and randomly oriented hematite plates form low-porosity clusters directly at the FM surface (Figure 6j).

The FMV of W17-1H is ~300 μm thick and contains two bands of hematite cataclasite with grain size, morphology, and fabric similar to W17-1G and W17-1J (Figures 7a and 7b). Cataclasite in the earlier layer exhibits a greater

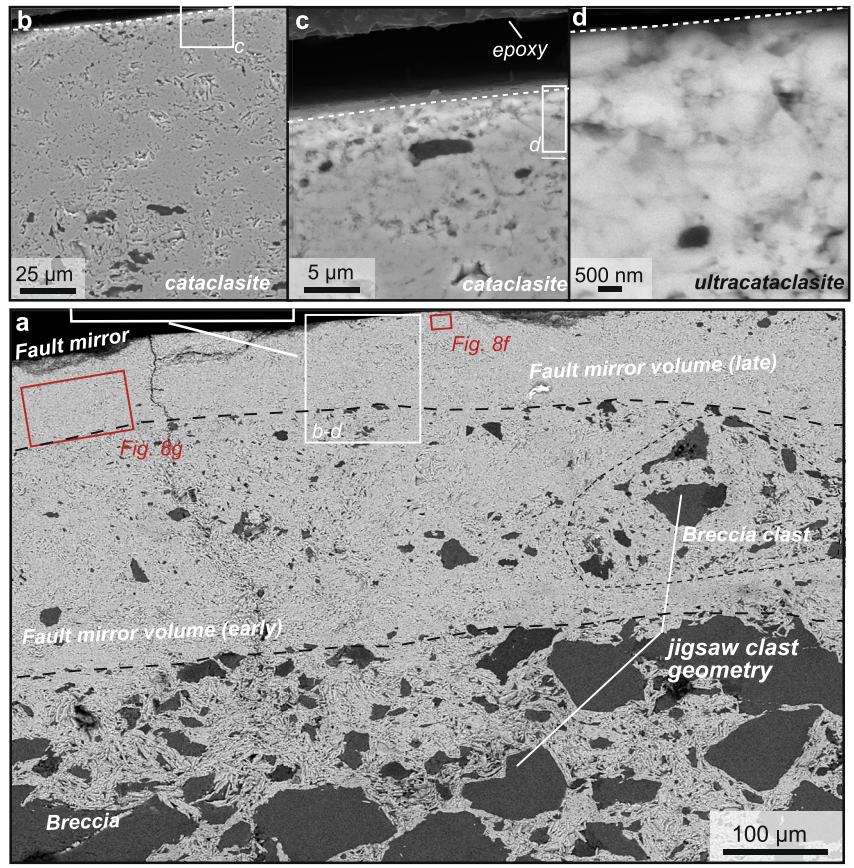

Figure 7. Sample W17-1H microstructures. (a) BSE image of hematite-cemented breccia and FMV. Note two (earlier and later) FMV generations (gen.). Clast of breccia outlined (black, dashed polygon). Red boxes show EBSD map areas (Figure 8). (b–d) BSE images at increasing magnification (left to right) of lower and upper FMV subdomain cataclasite and ultracataclasite, respectively. Symbology and annotations in all panels as in Figure 5.

proportion of wall-rock clasts and clasts of underlying breccia, identifiable by coarser hematite grain size and locally preserved jigsaw clast geometry (Figure 7a). The later, overlying band is ~80 μm thick (Figure 7a) and the uppermost ~5 μm of this layer is comprised exclusively of hematite ultracataclasite similar to that in W17-1G and W17-1J (Figures 7c and 7d). In two mounts made of this sample, we observed no other microstructure at the FM surface.

5.2. Electron Backscatter Diffraction

We present hematite EBSD results from seven areas within the FMV of our samples to further characterize microstructure, microtexture (e.g., crystallographic preferred orientation, CPO) and constrain hematite deformation mechanisms. We mapped at least two areas per sample, one representative of the broader FMV and a second near the FM surface (red boxes, Figures 5–7). From sample W17-1G, we acquired two maps of the upper FMV from near the FM surface, capturing both polygonal grain and ultracataclasite textures. In samples W17-1J and -1H, mapped areas capture polygonal grains adjacent to partially deformed plates and ultracataclasite, respectively.

5.2.1. Orientation Mapping and Crystallographic Preferred Orientations

Orientation (IPFx) maps and pole figures reveal additional textural heterogeneity in the FMV of each sample. In W17-1G, mapping across the transition from cataclasite to ultracataclasite reveals the latter is characterized by less intense average SPO and CPO (Figure 8a). Cataclasite consists of equant grains and high-aspect-ratio plates, with the latter generally increasing in parallelism with the FM toward the FM surface. Cataclasite hematite plates have CPO and <c> axes oriented both parallel and perpendicular to the FM surface (pole figures, Figure 8c). Overlying ultracataclasite forms a ~30 μm-thick layer of nanoparticles with no CPO and abundant no solution areas (in black; Figure 8a), likely related to porosity and fracturing (see Figure 5d).

Journal of Geophysical Research: Solid Earth
10.1029/2022JB025069

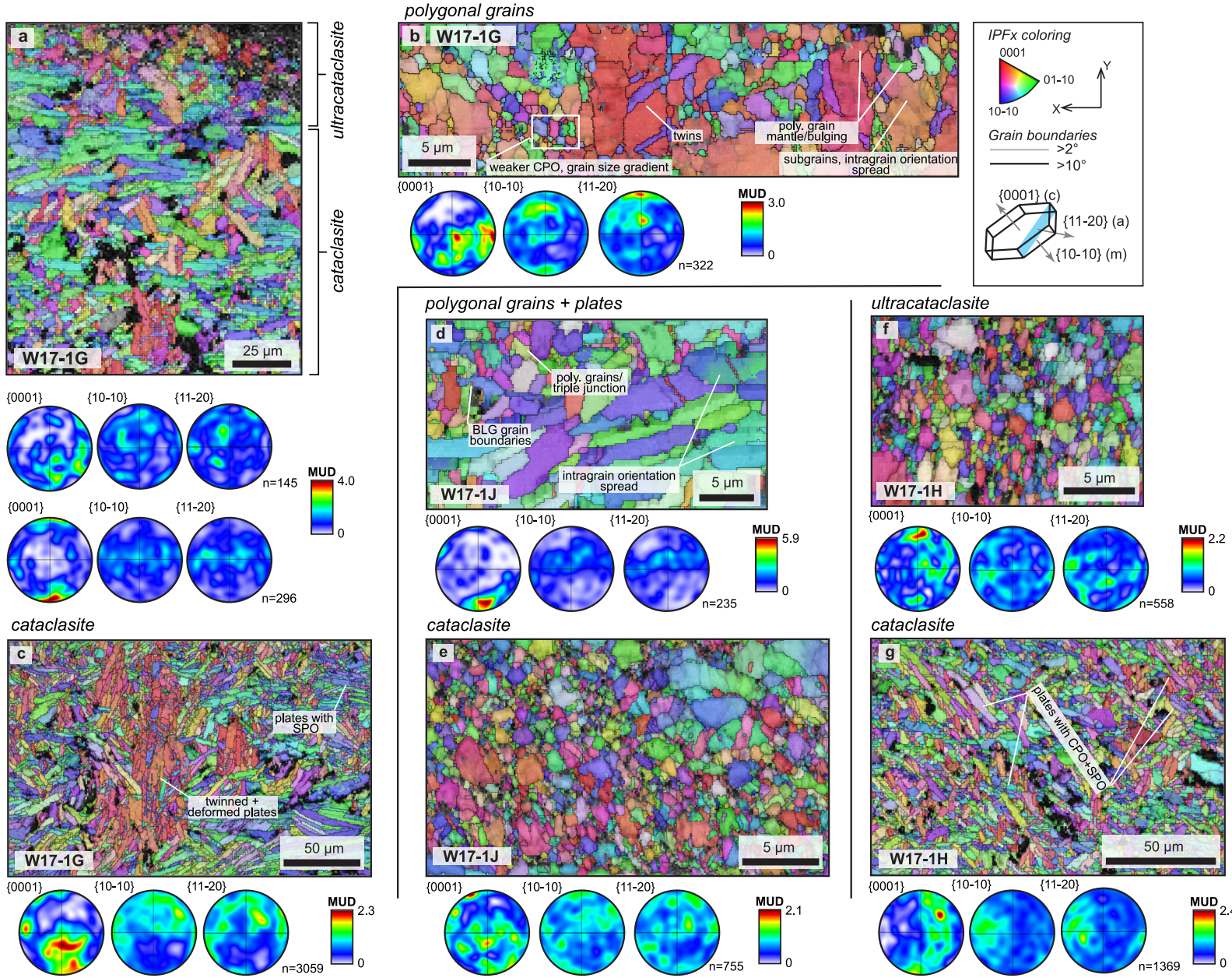

Figure 8. FMV inverse pole figure (in *x* direction, see upper right inset; IPFx) orientation maps and pole figures. (Sub)grain boundaries (≥2° and 10° misorientation, respectively) outlined in gray and black. See red boxes in Figures 5a, 6a, and 7a for map areas. Upper hemisphere equal-area projection pole figures of crystallographic axes (point-per-grain; *n*) with 15° half-width contouring. Color ramp shows multiples of uniform density (MUD). (a) FMV cataclasite to ultracataclasite transition in W17-1G. Pole figures show grains within ultracataclasite (upper row) and cataclasite (lower row). (b) W17-1G polygonal grains (near FM surface). (c) W17-1G FMV cataclasite and protocataclasite. (d) W17-1J polygonal grains and plates (near FM surface). (e) W17-1J FMV cataclasite. (f) W17-1H ultracataclasite (near FM surface). (g) W17-1H FMV cataclasite.

The EBSD maps capture two distinct textures associated with polygonal grains in W17-1G. The first is larger "parent" grains with polygonal grain mantles. Parent grains (Figure 8b) are variably twinned, contain subgrains (defined in this context as regions with misorientations between 2° and 10°), and exhibit modest intragranular orientation. Mantle grains show bulging grain boundaries with the parent grain and similar, but still distinct, grain orientations. The second, and more common, polygonal grain texture lacks discernible parent grains and has a greater spread in individual grain orientations (Figure 8b). These regions show systematically decreasing grain size with FM-perpendicular distance (Figure 8b), also observed in SEM images (Figure 5h). Moderate CPO across the entire map area is defined by <c> axes (sub)parallel to the FM, but with two maxima parallel and perpendicular to shear, and <a>/<m> axes parallel and perpendicular to the FM surface (pole figures, Figure 8b).

Hematite nearest to the FM surface of W17-1J exhibits strong CPO defined by both platy and polygonal grains (Figure 8d), with <c> axes sub-perpendicular to the FM surface and <a> and <m> axes forming FM surface-parallel girdle distributions (pole figures, Figure 8d). Some plates have intragranular orientation deviations and are mantled by polygonal grains. Polygonal grains directly beneath the FM surface are similarly oriented to underlying plates and exhibit rare bulging grain boundaries. Further from the FM surface and across the rest of the FMV, W17-1J is dominantly cataclasite with no CPO, although some larger, highly fractured plates are oriented parallel to the FM surface (Figure 8e).

FMV material nearest the W17-1H FM surface is distinct from the other two samples. Ultracataclasite exhibits no orientation deviations within grains and has no CPO (Figure 8f). The underlying lower FMV cataclasite has moderate CPO, with <c> axes forming a girdle distribution subperpendicular to slip and <a> and <m> axes weakly clustered subparallel to slip (pole figures, Figure 8g). Larger hematite plates define a weak CPO and SPO, but smaller cataclastic particles are randomly oriented (Figure 8g).

5.2.2. Misorientation Analyses

Misorientation analyses for FMV show intragranular deformation near the FM surface. Mis2mean maps from W17-1G show polygonal grains are largely misorientation (and strain) free. Intragranular misorientations, averaging up to ~15°, are concentrated within large plates in ultracataclasite (Figure 9a) and polygonal grain regions (Figure 9b). Polygonal grains in W17-1J are also mostly misorientation free, and some larger plates adjacent to polygonal grains show limited subgrain development (Figure 9c). W17-1H mis2mean maps of ultracataclastic grains show modest (<10°) intragranular misorientations focused at the tips of larger grains not apparent in orientation maps (Figure 9d). The proportion of neighbor-pair misorientation angles <10°, corresponding to subgrains, is greatest in W17-1G (polygonal grains and ultracataclasite, although the latter may partially be attributed to fracturing), lower in W17-1J, and lowest in W17-1H (Figure 9h). Strong peaks at 85° misorientation indicate *r*-twining in all samples (Figures 9e–9h; Avila et al., 2015).

We constructed MIPFs for neighbor-pair pixels and misorientations of 2–10° (i.e., subgrains) and 10–30° (Figures 9e–9h). These results show that the majority of misorientations for subgrains are accommodated about axes parallel to <c>, albeit at variable texture strength (e.g., low multiple of uniform density, or MUD, suggest only weak clustering in W17-1G ultracataclasite relative to other samples; Figure 9e). Polygonal grains in W17-1G and W17-1J show less intense maxima parallel to <m> and <a>, respectively (Figures 9f and 9g). W17-1H shows subgrain misorientations cluster parallel to <c>, but misorientations are otherwise random. In each sample, misorientation axis patterns for 10–30° angles mirror those at 2–10°, but are more muted and show a larger proportion of randomly oriented axes (Figures 9e–9h).

6. Discussion

6.1. Interpretation of Textural Observations and Deformation Mechanisms

6.1.1. Sequence of Hematite Precipitation and Deformation

The microstructures observed here are consistent with hematite FM development by repeated mineralization events and fault slip. Matrix-supported hematite breccia that crosscuts (Figure 3e), or entrains clasts of earlier hematite-cemented breccia (Figure 5a), record multiple episodes of brecciation and hematite precipitation. At field- and hand-sample scale, hematite-cemented breccia in all samples are cut by relatively homogenous hematite veins, reflecting additional fluid flow and hematite precipitation (Figures 2e, 3d, and 3h).

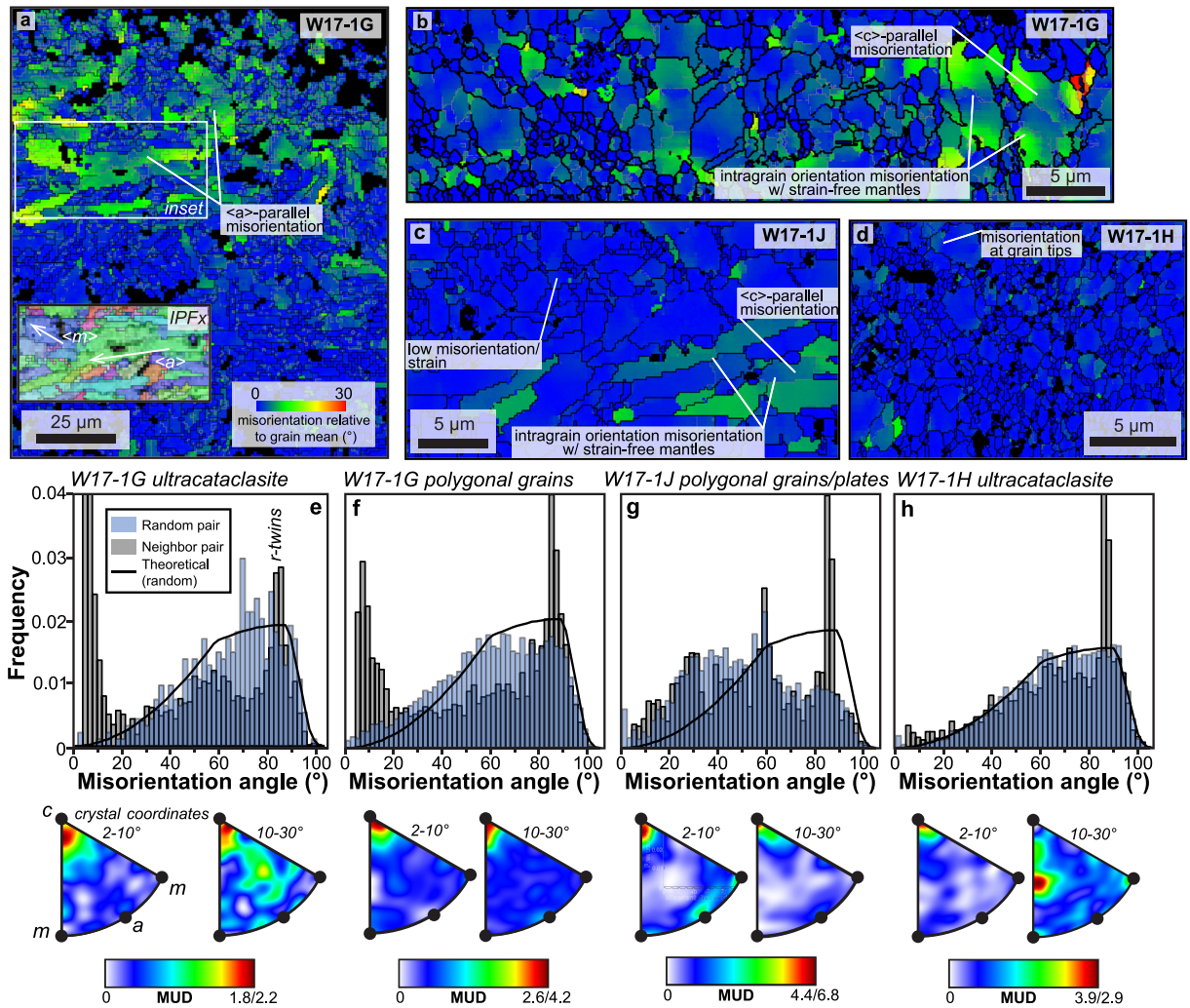

Figure 9. Misorientation analyses. Coloration is orientation difference of individual pixels within a grain relative to whole grain mean. (a) W17-1G FMV cataclasite/ultracataclasite transition (corresponds to Figure 8a). Inset is from IPFx map (Figure 8a). (b) W17-1G polygonal grains (corresponds to Figure 8b). (c) W17-1J polygonal grains and plates (corresponds to Figure 8d). (d) W17-1H ultracataclasite (corresponds to Figure 8f). (e–h) Histograms of misorientation angles between randomly selected grains (purple) and neighboring grains (gray) for map areas in 9a (e), 9b (f), 9c (g), and 9d (h). Black line shows theoretical random-pair distribution for a trigonal crystal system with no crystallographic preferred orientation. Peak at 85° misorientation in all samples likely corresponds to *r*-twins (Ávila et al., 2015). Corresponding misorientation inverse pole figures (MIPFs) show orientation of rotational axes around which misorientations are accommodated (i.e., misorientation axes) relative to crystallographic axes (denoted as black circles, labeled in (e)). MIPFs shown for misorientation magnitudes of subgrains (2°–10° misorientation) and low-angle grain boundaries (10°–30°) for comparison. Note color scale has different maximum MUD values for 2°–10° (left) and 10°–30° (right) MIPFs.

Hematite veins that crosscut breccia were reactivated to form the FMV during subsequent, localized deformation. Comminution of FMV hematite requires reactivation of pre-existing vein material (Figures 5a, 5c–5d, 6b, 6f, 7a, and 7b). A sharp contact between the FMV and underlying breccia; entrained, reworked breccia clasts in the FMV (Figure 7a); and differences in clast percentages in each layer, collectively support distinct precipitation events for the hematite-cemented breccia and veins that form the now-FMV (Figures 5a, 6a, and 7a). Shear deformation was almost entirely localized within the FMV, as evidenced by preservation of jigsaw-clast geometries (and thus negligible shear strain) in underlying breccia (Figures 3c, 3g, 5a, 6a, and 7a) and the lack of subsidiary slip surfaces away from the FM surface. The size of comminuted grains systematically decreases toward the FM surface in all samples, suggesting progressive strain localization within the FMV during slip (Figures 5b, 5e, 6b, and 7b). In general, hematite FM surfaces exhibit multiple striae with variable orientations (Figure 2f; Evans & Langrock, 1994; Evans et al., 2014), indicating more than one episode of slip occurred on the FMs. W17-1H has two distinct layers within the FMV, implying at least as many discrete episodes of deformation during FM development (Figure 7a). We do

not observe multiple FMV layers, internal slip surfaces, or striae in W17-1G and W17-1J (Figures 3a and 3d), and thus FMV microstructures in these samples likely reflect one slip event where our samples were taken.

Microstructures suggest additional, local hematite precipitation following deformation that generated the FMV in some samples. In W17-1J, high-porosity clusters of undeformed, euhedral hematite plates (Figure 6j) and specularite stringers (Figure 2d) on the FM surface reflect post-deformation precipitation of new hematite. Evidence for neoprecipitation in other samples is more ambiguous. W17-1H shows bands of high-aspect-ratio plates with SPO, inclined at ∼45° to the FM surface (Figure 8g) that may record either new hematite precipitation or heterogenous comminution with slip-induced, preferential alignment of platy grains in the deforming FMV. Approximately uniform IPFx coloring and broad clustering of <a> and <m> axes are indicative of CPO, compatible with neoprecipitation (for shear-induced grain alignment, we might anticipate SPO with aligned <c> axes, but randomly distributed <a> and <m> axes). In contrast, SPO in W17-1G cataclasite increases toward the FM surface (compare cataclasite domain <c> axes in Figure 8a with Figure 8c and note <a> and <m> axes are random). Thus, both neoprecipitation and heterogenous comminution with shear strain may contribute to hematite grain morphologies and fabric in FMV cataclasite, but to varying degrees in each sample.

6.1.2. Brittle and Plastic Deformation in the Fault Mirror Volume

Microstructures and EBSD data document evidence for brittle and plastic deformation mechanisms associated with strain localization and development of the FM surface. Cataclastic textures in the FMV imply brittle deformation and frictional slip at the grain-scale. Ultracataclasite in the upper FMV of all samples marks intense comminution and production of approximately equant nanoparticles (Figures 5d, 6h, and 7d). Reduction of CPO in ultracataclasite relative to underlying cataclasite reflects slip between comminuted grains, cataclastic granular flow, and likely "macroscopic" ductility in this uppermost portion of the FMV (Figures 8a and 8f; Borradaile, 1981; Hutter & Rajagopal, 1994).

We observe evidence for localized crystal plasticity in cataclastic layers. In W17-1G, EBSD mapping shows intragranular misorientation and subgrain density increase toward the FM surface, particularly in larger platy grains (Figure 9a). Some boundaries marked as separating subgrains may be related to fracturing and associated difficulties in indexing porous material. However, rare survivor hematite plates near the ultracataclasite-cataclasite boundary have smoothly varying misorientation on the order of 15°, suggestive of localized, incipient crystal plastic deformation within this layer. Cataclastic flow and pervasive intragranular fracturing in the upper FMV yield random CPO and subgrain misorientation axes relative to other samples (compare MUD values in Figures 9e–9h), complicating interpretations of exact deformation mechanisms in our samples. However, consistent <a>- and <m>-parallel misorientation gradients in larger plates are most compatible with the {a}<m> prism slip system documented in hematite (see Figure 9a and IPFx inset; Hennig-Michaeli & Siemes, 1982). Hematite torsion experiments at strain rates of 10^{-5} s^{-1} indicate prism slip is activated at temperatures of ≥400–600°C (Siemes et al., 2008), and we thus suggest temperatures of at least this magnitude were attained in W17-1G ultracataclasite. W17-1H ultracataclasite similarly shows local misorientations in larger grains, although not as well developed, implying incipient crystal plastic deformation but perhaps at lower overall temperatures than W17-1G (Figure 9d).

Regions of polygonal grains in W17-1G and W17-1J record evidence for crystal plasticity. Polygonal grains that mantle large hematite plates with intragranular misorientations >15–30° and subgrains are similar to core and mantle structures reported in a variety of dynamically recrystallized rock types, including hematite (Figures 6i, 8b, 8d, 9b, 9b, and 9c; e.g., Schmid et al., 1980; Siemes et al., 2003, 2011; Stipp et al., 2002). This microstructure and CPO development in these grains are consistent with dislocation migration and crystal plastic deformation. Grain mantles free of misorientation may reflect some component of recovery-accommodated recrystallization, but is complicated by post-deformation annealing (discussed below). Intragranular misorientation gradients parallel to <c> and local, moderate CPO are compatible with basal ((c)<a>) slip in these mantling polygonal grains (Figures 8b and 9b; Ferreira et al., 2016; Siemes et al., 2008). Weaker clusters of subgrain misorientation axes parallel to <m> are also compatible with basal slip, but those parallel to <c> reflect either twist-type (rotation about the <c> axes) dislocations during basal glide or a component of prism slip (Figure 9f; Lloyd, 2004; Mendes & Lagoeiro, 2012; Rosiere et al., 2001). Of note is that <c> axes in W17-1G are dominantly parallel and perpendicular to the shearing direction (Figure 8b), counter to the expectation for basal slip (cf. Ferreira et al., 2016) and contrary to other evidence this is the dominant slip system. Similar CPO patterns have been reported in experimentally deformed hematite and olivine, interpreted to reflect grain boundary sliding processes (GBS; Précigout & Hirth, 2014; Siemes et al., 2011, 2010). By comparison to hematite deformation experiments

where basal slip and potential GBS are activated, these core-mantle polygonal grain textures imply temperatures ≥600–800°C and ≥900–1000°C, respectively (Siemes et al., 2008, 2003, 2011, 2010).

Regions of polygonal grains within 20 μm of the surface of W17-1G and W17-1J characterized by a pronounced grain size gradient, less intense CPO, pervasive triple junctions, and lack of intragranular misorientations (e.g., W17-1G; Figures 8b and 9b) are consistent with grain growth by sintering and annealing (e.g., Heilbronner & Tullis, 2002) along an FM-perpendicular thermal gradient as observed in other experimental and natural FMs (Ault et al., 2019; Pozzi et al., 2018). Given that polygonal textures also developed on tips of FMV plates that intrude into these broader regions of polygonal grains, we infer annealing occurred post-plastic deformation and was static or quasi-static (Figures 5h and 5i). Annealing is a grain size sensitive process, which may explain why only larger grains preserve evidence of dislocation-assisted deformation. Based on hematite dry heating experiments characterized by grain growth and polygonal grain morphology development, these textures suggest temperatures >1000°C were ultimately achieved in this region of W17-1G (Siemes et al., 2008, 2003; Vallina et al., 2014). Similar, although less common, textures and misorientation patterns indicative of plastic deformation and annealing are present in W17-1J. Annealed grains for this sample show sub-polygonal morphologies more akin to experimental products heated to ∼800°C (Figure 4h; Vallina et al., 2014), and we thus infer similar deformation mechanisms but at overall lower temperatures for this sample.

6.2. Seismic Slip Along Hematite Fault Mirrors

Evidence for crystal plastic deformation and high-temperature annealing in the FMV suggests these WFZ hematite FMs textures attained high temperatures during small paleoearthquakes. Prior hematite (U-Th)/He dates from a broad inventory of FM samples and complementary host rock apatite (U-Th)/He data suggest this seismic slip occurred at depths <2 km (Ault et al., 2015; McDermott et al., 2017), and thus far below the ambient temperatures where steady-state plasticity typically occurs (Siemes et al., 2011). Our microstructural observations suggest FMs attained transient, elevated temperatures through friction-generated heat, unique to seismic slip rates (e.g., Rowe & Griffith, 2015), within a narrow portion of the uppermost FMV and directly beneath the FM surface. Comparison of documented FM microstructures to hematite deformation and dry heating experimental products suggests coseismic temperatures ≥400–1000°C (Siemes et al., 2008, 2010; Vallina et al., 2014). These temperatures are minimum estimates given prior experiments were conducted at much slower strain rates and longer durations than those typical for seismic slip (e.g., Rowe & Griffith, 2015). Our results are also consistent with prior study of WFZ hematite FMs that document evidence for coseismic temperature rise (Ault et al., 2015; Evans et al., 2014; McDermott et al., 2017).

Coseismic temperatures varied between FM surfaces, and along a single FM surface during the same slip event. Variations in temperature rise parallel and perpendicular to the FM surface are correlated with fault properties (Figure 4). We observe ultracataclasite and likely temperatures on the order of ∼400°C in all samples where the FMV is ∼80–100 μm thick (Figures 4a, 4b, 5a–5d, and 6e–6f). Sample W17-1H exhibits only cataclastic microstructures and, although temperatures may have varied across this FM, they likely did not exceed 400°C at any point. Temperatures documented on W17-1J are locally higher and range from ≥600°C to 800°C based on limited crystal plasticity by basal slip and sub-polygonal grain morphologies related to annealing (Siemes et al., 2008; Vallina et al., 2014). We only observe these textures where the upper FMV is ∼25 μm thick (Figures 6a–6d), and the highest temperatures implied by annealed grains being restricted to an ∼5 μm-thick layer at the FM surface (Figures 6g and 6h). The greatest peak temperatures and presence of FM surface-perpendicular and -parallel thermal gradients are documented on W17-1G. Along this FM, surface peak temperatures vary from ∼≥400°C (ultracataclasite) to >1000°C (polygonal grains) over sub-mm scales (Figures 5a, 5e–5g, 8b, 9b, and 9f). Polygonal grains are observed where the FMV is locally >280 μm thick, but restricted to a <10 μm-thick zone directly beneath the FM surface and at a clear geometric asperity (Figures 4d, 5a, and 5e–5g). Although only one observation, this suggests constructive effects of both strain localization and asperity flash heating processes leading to extreme temperature rise (e.g., Platt et al., 2014).

6.3. Fault Mirror Evolution and Interpreted Weakening Mechanisms

We integrate field, microstructural, and timing constraints into a conceptual model for the evolution of a generalized hematite FM that captures the interplay between hematite precipitation and breccia vein formation, fault

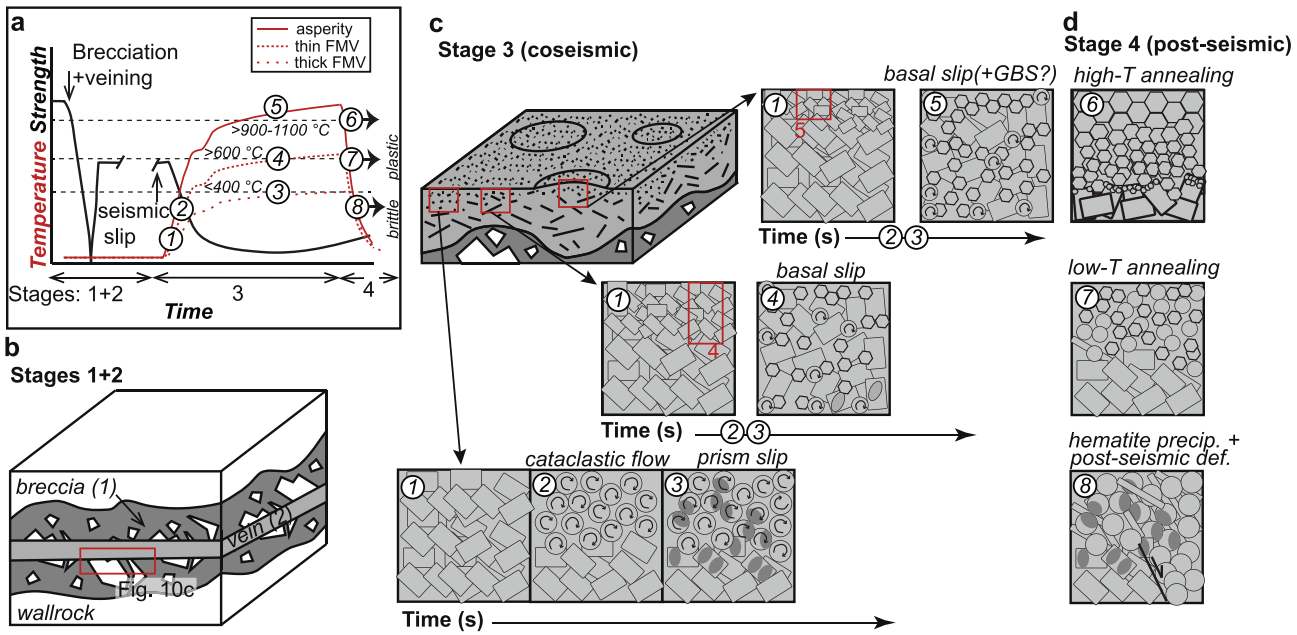

Figure 10. Conceptual model of hematite FM evolution. (a) Schematic host rock and FM-averaged strength (black) and temperature (red) evolution. Temperature curves correspond to regions of thick FMV (dotted), thin FMV (dashed), and at geometric asperity (solid). Numbers denote textural stages depicted in (b–d). (b) Block diagram showing repeated brecciation with hematite cement (Stage 1) and hematite veining (Stage 2). (c) Block diagram showing FMV textural evolution during Stage 3 for regions with different FMV thickness and FM surface topography during seismic slip. Bold circled letters for each panel link to curves in panel (a). (d) Stage 4 post-seismic textural evolution of polygonal grain growth and annealing, precipitation of new hematite plates, and localized deformation and offset of the FMV along shear fractures.

reactivation, strain localization, and ultimately dynamic weakening and seismogenesis using observations from all samples (Figure 10). This model must account for variable peak coseismic temperatures of ~≥400°C to ≥1000°C, both between and along individual hematite FM surfaces. Coseismic temperature rise depends on displacement, slip velocity, shear zone thickness, and shear stress, all of which may vary across a single fault surface and evolve with slip (Beroza & Mikumo, 1996; Bouchon, 1997; Cardwell, 1978; Rice, 2006; Shervais & Kirkpatrick, 2016). Although many of these factors are difficult to constrain in our samples, gradational and overprinting textures in the FMV, FMV thickness, and fault surface topography all correlate to variations in inferred local peak temperature—suggesting the initial state and(or) evolution of these factors are of primary importance in controlling spatially variable coseismic temperatures. Our conceptual model depicts FM textural and mechanical evolution through this lens. We compare textural stages to prior experimental work to infer relative changes in temperature and static (Stages 1 and 2), FM-averaged dynamic (Stage 3), and post-seismic (Stage 4) fault strength (Figure 10a).

Stages 1 and 2 correspond to early, multi-stage hematite precipitation and vein formation (Figure 10b). The key element of stages 1 and 2 is long-term, localized weakening of gneissic host rock through episodic hematite precipitation that ultimately introduces abundant cm to sub-mm rheological discontinuities (Figure 10b). Micron-scale specular hematite, similar to initial vein material here, has a slightly lower coefficient of friction than crystalline rock and shows subtle dynamic weakening behavior at laboratory seismic slip rates (Byerlee, 1978; Calzolari et al., 2020), thereby facilitating strain localization and future seismic slip.

Stage 3 corresponds to seismic slip (Figure 10c). Initial deformation may have been distributed across the FMV and breccia, given rare breccia-penetrating Riedel-type shears (Figure 2b), but was apparently quickly localized to the FMV. This is supported by preservation of breccia clast jigsaw geometries, requiring limited overall shear in the breccia. Our microstructural observations show further localization in the FMV, with EBSD data implying grain rolling, macroscopic ductility, and overall weakening in this layer (Figures 8a, 8e, 8f, and 10c). Rotary shear apparatus experiments show strain localization is concomitant with early dynamic weakening (Pozzi et al., 2019; Smith et al., 2015). In our samples, extreme comminution and granular flow mechanisms imply low dynamic

shear strength, similar to nanoparticle lubrication processes documented in experimental faults (Figure 10c, panels 1 and 2; Han et al., 2011; Verberne et al., 2014).

As slip proceeds, shear zone width locally narrows to <100 μm and coseismic temperatures ≥400°C are achieved, leading to the onset of crystal plasticity and prism slip (Figures 10a and 10c, panels 1–3). Where shear zone narrows to a width <20 μm, temperatures ≥600°C promote a transition to basal slip and more pervasive plastic deformation (Figures 10a and 10c, panels 1–4). The highest temperatures (>1000°C) are achieved where the shear zone is both narrow and underlies geometric asperities (Figures 5a and 10a), as shown in Figure 10c (panels 1–5). Regions of the slipping surface dominated by crystal plasticity experience viscous flow and low average dynamic shear strength (Figure 10a; e.g., Ohl et al., 2021; Pozzi et al., 2019; Siman-Tov et al., 2015). Geometric asperities are loci of shear stress, resulting in extreme heating and weakening (Rice, 2006). Asperity flash heating as a dynamic weakening mechanism on WFZ hematite FMs is consistent with prior study (Ault et al., 2015; Evans et al., 2014; McDermott et al., 2017). In all cases, plastic deformation mechanisms operate on the order of seconds or less before FMV temperatures fall below those required to activate plastic deformation (e.g., Spagnuolo et al., 2015).

Post-seismic annealing and(or) hematite precipitation contribute to healing and recovery of fault strength (Stage 4; Figures 10a and 10d). Sintering and annealing of hematite grains in regions where temperatures exceed 800–1000°C (Figure 10d, panels 6 and 7) may result in net strength recovery (Wright, 1976), and these processes have been attributed to strength recovery in other hematite FMs (Ault et al., 2019). In at least W17-1G, overprinting microstructural relations between polygonal grains and underlying plates confirm this process persisted post-slip (Figures 5h and 5i). In cataclastic regions of the FMV, we observe evidence for additional, post-seismic hematite precipitation (Figure 10d, panel 8), at least in W17-1J (Figure 6j). This is compatible with more traditional views of fault healing (e.g., Sibson, 1992). Locally, shear fractures cut and offset the FMV (e.g., W17-1J; Figures 6e and 10d, panel 8). These features are enigmatic, but along with some evidence for synkinematic precipitation of hematite with CPO (e.g., W17-1H; Figure 8g), suggest a possible spectrum of afterslip- or relaxation-like deformation processes.

7. Implications for Seismic Processes

7.1. Structural Context of Hematite FM Seismicity

Hematite FMs archive episodic hematite precipitation, fault reactivation, and shallow nano-to microseismicity within the broader WFZ. Normal slip on FMs studied here and (U-Th)/He constraints for post-4.5 Ma deformation (Ault et al., 2015; McDermott et al., 2017) on other FMs are kinematically and temporally compatible with extension in the WFZ. However, multiple structural regimes have impacted our study area (i.e., Cretaceous contraction; Yonkee et al., 2019). Prior (U-Th)/He data from specularite veins (located ∼80 m and 2 km from the outcrop studied here) range from Cretaceous to Miocene (McDermott et al., 2017). Normal and oblique reverse slip (the latter potentially reflecting Cretaceous contraction) in the broader hematite FM network also suggest the possibility of protracted hematite precipitation and FM development (Figures 2b and 2f).

Hematite FMs occasionally preserve field evidence for <1–2 cm of separation (Figure S1 in Supporting Information S1), although multiple striae on many FMs (e.g., Figure 2f) imply individual slip events had lower displacement. Evans et al. (2014) and McDermott et al. (2017) argued WFZ hematite FMs accommodated tens of micrometers to a few mm of slip in any given event based on the sub-m lengthscale of FM patches (e.g., Figures 2c–2f) and typical seismological scaling relations (Boettcher et al., 2009). We similarly suggest the hematite FMs studied here likely accommodated μm- to mm-scale slip during each event, corresponding to nano- to microseismicity (cf. Eaton et al., 2016). Although the number of samples investigated in detail here is limited, they are representative of the broader network of 10^4 to $>10^5$ hematite FMs defining voluminous off-fault damage of the WFZ (Evans & Langrock, 1994; McDermott et al., 2017). Hematite FMs decorate the damage zones of mesoscale faults that presumably accommodate larger earthquakes, and FMs plausibly reflect aftershock or foreshocks in association with larger ruptures through these structures or the broader WFZ (cf. Ault et al., 2015).

7.2. Strain Localization and Coseismic Temperature Rise

We document coseismic paleotemperatures on the order of ≥400°C to >1000°C related to extreme strain localization and the thickness of pre-slip vein material that forms the FMV. Coseismic temperature rise, ΔT, is given by Lachenbruch (1986):

$$\Delta T = \frac{\mu \sigma D}{2\rho c} \quad \text{for} \quad \frac{\mathrm{w}}{\sqrt{4\alpha t}} > 1 \tag{1}$$

$$\Delta T = \frac{\mu \sigma \mathrm{v} \sqrt{t}}{\rho c \sqrt{\pi \alpha}} \quad \text{for} \quad \frac{w}{\sqrt{4\alpha t}} \to 0$$

where μ is the coefficient of friction, σ is normal stress, D is coseismic displacement, ρ is density, c is heat capacity, w is slip zone half-width, α is thermal diffusivity, v is slip velocity, and t is time. Equation 1 shows that coseismic temperature rise is nonlinear, with the rate of ΔT increasing when $w \leq \sqrt{\pi \alpha \mathrm{t}}$. Parameterizing Equation 1 is difficult, particularly for rough surfaces with poorly constrained displacement such as our hematite FMs, but we calculate the shear zone half-widths over which ΔT is anticipated to be more efficient. For $\alpha = 1.55 \times 10^{-5}$ m^2/s (Robertson, 1988) and $t = 10$ μs to 1 ms (i.e., assuming $D = 10$ μm to 1 mm and slip velocity of 1 m/s; Rowe & Griffith, 2015), w ranges from ~20 to 220 μm. These values are remarkably consistent with observed thickness variations in FMV material. We thus suggest that for our small-displacement hematite FMs where only modest temperature rise is expected, the initial shear zone thickness set by precursor vein material comprising the FMV plays a key role in facilitating rapid temperature rise, thermally activated weakening, and ultimately, seismicity. This calculation highlights the influence of strain localization via pre-existing fault structure on seismicity.

Hematite FMs provide a record of past coseismic temperature rise and associated deformation mechanisms that vary on the microscale. Variable temperatures and activated crystal plastic deformation mechanisms imply flow stress differs across FM surfaces (Siemes et al., 2008), potentially related to variation of local normal stress and heterogeneity in the FMV. This is compatible with other studies of exhumed faults, but further extends the length scales over which dynamic weakening mechanisms and coseismic stress may vary on a single slip surface (Coffey et al., 2019; Kirkpatrick & Shipton, 2009). Healing mechanisms ranging from neoprecipitation to grain sintering imply local heterogeneities in post-seismic strength recovery. Improved documentation of the lengthscales over which dynamic weakening mechanisms vary on natural fault surfaces has direct implications for building realistic models of fault rheology and slip (cf. Cornelio et al., 2022).

Although these FMs did not accommodate large-magnitude earthquakes, the rich diversity of microstructures and paleotemperature evidence is preserved precisely because of small displacements and limited overprinting. Generally, the early stages of seismic slip (i.e., before significant slip has accumulated and overprinted earlier microstructures) are difficult to simulate experimentally given typical stiffness of shear apparatuses, which complicate accelerating to seismic velocities over short displacements (with some notable exceptions, e.g., Hayward et al., 2016). Study of WFZ hematite FMs, and other small faults, may serve to fill this gap. Our observations help capture the spatiotemporal distribution of deformation and dynamic weakening processes active over the first few μm to mm of slip in larger magnitude earthquakes.

8. Conclusions

We document the textural and thus thermal and mechanical evolution of WFZ hematite FMs. Field, microscopy, and EBSD observations reveal FMs comprise hematite-cemented breccia and veins, which formed during multiple hematite precipitation events and were preferentially reactivated to accommodate seismic slip. The FMV comprises diverse grain morphologies including cataclasite, ultracataclasite, and recrystallized and annealed grains. Microstructural and EBSD patterns constrain deformation mechanisms ranging from brittle to plastic and imply temperatures varied from ≥400°C to ≥1000°C, across individual FM surfaces over the microscale and between FM surfaces. Peak coseismic temperatures correlate with FMV thickness and FM surface roughness, highlighting the role of intrinsic fault properties and progressive strain localization play in controlling the distribution of transient, elevated coseismic temperatures on these small, thin slip surfaces.

Our results have implications for earthquake mechanics within the WFZ and potentially other major fault systems at shallow depth. First, we argue that given the small-displacements along hematite FMs, inferred fault slip temperatures

are more achievable with an initially thin deforming zone. This highlights how prior veining facilitates future seismic slip on our studied samples, but points to the importance of strain localization in other fault systems with thin slip surfaces. Second, our observations highlight the sub-mm length scales over which dynamic weakening mechanisms, coseismic temperatures, and stress may vary on a single slip surface and during a single slip event. In this regard, the small displacements accommodated on WFZ FMs are particularly advantageous for preserving microstructural evolution, which may mirror processes operative during the first few μm to mm of slip in larger magnitude earthquakes.

Data Availability Statement

All information used to derive the conclusions of this work are in the main text and Supporting Information. The Supporting Information and unprocessed EBSD data files are available at figshare.com (https://doi.org/10.6084/m9.figshare.21669632.v1).

Acknowledgments
This work was supported by an NSF CAREER EAR-1654628 to AKA, USU Dissertation Enhancement grant to RGM, and NSF EAR-1419828 to AKA and JPE. RGM was supported by the U.S. Geological Survey Mineral Resources Program during writing and editing of the manuscript. All EBSD data were processed with a free license of *AztecCrystal-Timed*, provided by Oxford Instruments. Our manuscript greatly benefitted from constructive reviews by Randy Williams, Giacomo Pozzi, Ben Melosh, and an anonymous reviewer. The authors thank Editor Isabelle Manighetti and the Associate Editor for editorial handling and additional comments that improved the manuscript. Any use of trade, firm, or product names is for descriptive purposes only and does not imply endorsement by the U.S. Government.

References

Arabasz, W. J., Burlacu, R., & Pechmann, J. C. (2017). *Earthquake database for Utah Geological Survey Map 277: Utah earthquakes (1850–2016) and Quaternary faults (OFR-667)*. Utah Geological Survey.

Aretusini, S., Núñez-Cascajero, A., Spagnuolo, E., Tapetado, A., Vázquez, C., & Di Toro, G. (2021). Fast and localized temperature measurements during simulated earthquakes in carbonate rocks. *Geophysical Research Letters*, *48*(9), e2020GL091856. https://doi.org/10.1029/2020gl091856

Armstrong, E. M., Ault, A. K., Bradbury, K. K., Savage, H. M., Polissar, P. J., & Thomson, S. N. (2022). A multi-proxy approach using zircon (U-Th)/He thermochronometry and biomarker thermal maturity to robustly capture earthquake temperature rise along the Punchbowl Fault, California. *Geochemistry, Geophysics, Geosystems*, *23*(4). https://doi.org/10.1029/2021gc010291

Ault, A. K. (2020). Hematite fault rock thermochronometry and textures inform fault zone processes. *Journal of Structural Geology*, *133*, 104002. https://doi.org/10.1016/j.jsg.2020.104002

Ault, A. K., Jensen, J. L., McDermott, R. G., Shen, F. A., & Van Devener, B. R. (2019). Nanoscale evidence for temperature-induced transient rheology and postseismic fault healing. *Geology*, *47*(12), 1203–1207. https://doi.org/10.1130/g46317.1

Ault, A. K., Reiners, P. W., Evans, J. P., & Thomson, S. N. (2015). Linking hematite (U-Th)/He dating with the microtextural record of seismicity in the Wasatch fault damage zone, Utah, USA. *Geology*, *43*(9), 771–774. https://doi.org/10.1130/g36897.1

Avila, C. F., Lagoeiro, L., Ferriera Barbosa, P., & Graça, L. (2015). EBSD analysis of rhombohedral twinning in hematite crystals of naturally deformed iron formations. *Journal of Applied Crystallography*, *48*(1), 212–219. https://doi.org/10.1107/s1600576714025928

Beroza, G. C., & Mikumo, T. (1996). Short slip duration in dynamic rupture in the presence of heterogeneous fault properties. *Journal of Geophysical Research: Solid Earth*, *101*(B10), 22449–22460. https://doi.org/10.1029/96jb02291

Boettcher, M. S., McGarr, A., & Johnston, M. (2009). Extension of Gutenberg-Richter distribution to Mw −1.3, no lower limit in sight. *Geophysical Research Letters*, *36*(10), L10307. https://doi.org/10.1029/2009gl038080

Borradaile, G. J. (1981). Particulate flow of rock and the formation of cleavage. *Tectonophysics*, *72*(3–4), 305–321. https://doi.org/10.1016/0040-1951(81)90243-2

Bouchon, M. (1997). The state of stress on some faults of the San Andreas system as inferred from near-field strong motion data. *Journal of Geophysical Research: Solid Earth*, *102*(B6), 11731–11744. https://doi.org/10.1029/97jb00623

Bruhn, R. L., Parry, W. T., Yonkee, W. A., & Thompson, T. (1994). Fracturing and hydrothermal alteration in normal fault zones. *Pure and Applied Geophysics*, *142*(3), 609–644. https://doi.org/10.1007/bf00876057

Bryant, B. (1988). *Geology of the Farmington Canyon Complex* (Vol. 1476, p. 54). U.S. Geological Survey Professional Paper.

Byerlee, J. (1978). Friction of rocks. In *Rock friction and earthquake prediction* (pp. 615–626). Birkhäuser.

Calzolari, G., Ault, A. K., Hirth, G., & McDermott, R. G. (2020). Hematite (U-Th)/He thermochronometry detects asperity flash heating during laboratory earthquakes. *Geology*, *48*(5), 514–518. https://doi.org/10.1130/g46965.1

Cardwell, R. K., Chinn, D. S., Moore, G. F., & Turcotte, D. L. (1978). Frictional heating on a fault zone with finite thickness. *Geophysical Journal International*, *52*(3), 525–530. https://doi.org/10.1111/j.1365-246x.1978.tb04247.x

Chester, F. M., Evans, J. P., & Biegel, R. L. (1993). Internal structure and weakening mechanisms of the San Andreas fault. *Journal of Geophysical Research: Solid Earth*, *98*(B1), 771–786. https://doi.org/10.1029/92jb01866

Chester, F. M., & Logan, J. M. (1986). Implications for mechanical properties of brittle faults from observations of the Punchbowl Fault zone, California. *Pure and Applied Geophysics*, *124*(1), 79–106. https://doi.org/10.1007/bf00875720

Coffey, G. L., Savage, H. M., Polissar, P. J., Rowe, C. D., & Rabinowitz, H. S. (2019). Hot on the trail: Coseismic heating on a localized structure along the Muddy Mountain fault, Nevada. *Journal of Structural Geology*, *120*, 67–79. https://doi.org/10.1016/j.jsg.2018.12.012

Cornelio, C., Spagnuolo, E., Aretusini, S., Nielsen, S., Passelègue, F., Violay, M., et al. (2022). Determination of parameters characteristic of dynamic weakening mechanisms during seismic faulting in cohesive rocks. *Journal of Geophysical Research: Solid Earth*, *127*(7), e2022JB024356. https://doi.org/10.1029/2022jb024356

Crittenden, M. D., & Sorensen, M. L. (1985). *Geologic map of the Mantua quadrangle and part of the Willard quadrangle*. U.S. Geological Survey.

De Paola, N., Holdsworth, R. E., Viti, C., Collettini, C., & Bullock, R. (2015). Can grain size sensitive flow lubricate faults during the initial stages of earthquake propagation? *Earth and Planetary Science Letters*, *431*, 48–58. https://doi.org/10.1016/j.epsl.2015.09.002

Dieterich, J. H. (1992). Earthquake nucleation on faults with rate-and state-dependent strength. *Tectonophysics*, *211*(1–4), 115–134. https://doi.org/10.1016/0040-1951(92)90055-b

Di Toro, G., Han, R., Hirose, T., De Paola, N., Nielsen, S., Mizoguchi, K., et al. (2011). Fault lubrication during earthquakes. *Nature*, *471*(7339), 494–498. https://doi.org/10.1038/nature09838

Di Toro, G., Hirose, T., Nielsen, S., Pennacchioni, G., & Shimamoto, T. (2006). Natural and experimental evidence of melt lubrication of faults during earthquakes. *Science*, *311*(5761), 647–649. https://doi.org/10.1126/science.1121012

DuRoss, C. B., Personius, S. F., Crone, A. J., Olig, S. S., Hylland, M. D., Lund, W. R., & Schwartz, D. P. (2016). Fault segmentation: New concepts from the Wasatch fault zone, Utah, USA. *Journal of Geophysical Research: Solid Earth*, *121*(2), 1131–1157. https://doi.org/10.1002/2015jb012519

Eaton, D. W., van der Baan, M., & Ingelson, A. (2016). Terminology for fluid-injection induced seismicity in oil and gas operations. *Canadian Journal of Exploration Geophysics Recorder*, *41*(04).

Ehlers, T. A., Willett, S. D., Armstrong, P. A., & Chapman, D. S. (2003). Exhumation of the central Wasatch Mountains, Utah: 2. Thermokinematic model of exhumation, erosion, and thermochronometer interpretation. *Journal of Geophysical Research: Solid Earth*, *108*(B3). https://doi.org/10.1029/2001jb001723

Evans, J. P., & Langrock, H. (1994). Structural analysis of the Brigham City-Weber segment boundary zone, Wasatch normal fault, Utah: Implications for fault growth and structure. *Pure and Applied Geophysics*, *142*(3), 663–685. https://doi.org/10.1007/bf00876059

Evans, J. P., Prante, M. R., Janecke, S. U., Ault, A. K., & Newell, D. L. (2014). Hot faults: Iridescent slip surfaces with metallic luster document high-temperature ancient seismicity in the Wasatch fault zone, Utah, USA. *Geology*, *42*(7), 623–626. https://doi.org/10.1130/g35617.1

Faber, C., Rowe, C. D., Miller, J. A., Fagereng, Å., & Neethling, J. H. (2014). Silica gel in a fault slip surface: Field evidence for palaeo-earthquakes? *Journal of Structural Geology*, *69*, 108–121. https://doi.org/10.1016/j.jsg.2014.09.021

Faulkner, D. R., Lewis, A. C., & Rutter, E. H. (2003). On the internal structure and mechanics of large strike-slip fault zones: Field observations of the Carboneras fault in southeastern Spain. *Tectonophysics*, *367*(3–4), 235–251. https://doi.org/10.1016/s0040-1951(03)00134-3

Ferreira, F., Lagoeiro, L., Morales, L. F., de Oliveira, C. G., Barbosa, P., Ávila, C., & Cavalcante, G. C. (2016). Texture development during progressive deformation of hematite aggregates: Constraints from VPSC models and naturally deformed iron oxides from Minas Gerais, Brazil. *Journal of Structural Geology*, *90*, 111–127. https://doi.org/10.1016/j.jsg.2016.07.009

Goddard, J. V., & Evans, J. P. (1995). Chemical changes and fluid-rock interaction in faults of crystalline thrust sheets, northwestern Wyoming, USA. *Journal of Structural Geology*, *17*(4), 533–547. https://doi.org/10.1016/0191-8141(94)00068-b

Goldsby, D. L., & Tullis, T. E. (2011). Flash heating leads to low frictional strength of crustal rocks at earthquake slip rates. *Science*, *334*(6053), 216–218. https://doi.org/10.1126/science.1207902

Han, R., Hirose, T., Shimamoto, T., Lee, Y., & Ando, J. I. (2011). Granular nanoparticles lubricate faults during seismic slip. *Geology*, *39*(6), 599–602. https://doi.org/10.1130/g31842.1

Hayward, K. S., Cox, S. F., Fitz Gerald, J. D., Slagmolen, B. J., Shaddock, D. A., Forsyth, P. W., et al. (2016). Mechanical amorphization, flash heating, and frictional melting: Dramatic changes to fault surfaces during the first millisecond of earthquake slip. *Geology*, *44*(12), 1043–1046. https://doi.org/10.1130/g38242.1

Heilbronner, R., & Tullis, J. (2002). The effect of static annealing on microstructures and crystallographic preferred orientations of quartzites experimentally deformed in axial compression and shear. *Geological Society, London, Special Publications*, *200*(1), 191–218. https://doi.org/10.1144/gsl.sp.2001.200.01.12

Hennig-Michaeli, C., & Siemes, H. (1982). Experimental deformation of hematite crystals between 25°C and 400°C at 400 MPa confining pressure. In W. Schreyer (Ed.), *High pressure research in geoscience* (pp. 133–150). Schweizerbart'sche Verlagsbuchhandlung.

Houser, L. M., Ault, A. K., Newell, D. L., Evans, J. P., Shen, F. A., & Van Devener, B. R. (2021). Nanoscale textural and chemical evolution of silica fault mirrors in the Wasatch fault damage zone, Utah, USA. *Geochemistry, Geophysics, Geosystems*, *22*(3), e2020GC009368. https://doi.org/10.1029/2020gc009368

Hutter, K., & Rajagopal, K. R. (1994). On flows of granular materials. *Continuum Mechanics and Thermodynamics*, *6*(2), 81–139. https://doi.org/10.1007/bf01140894

Kirkpatrick, J. D., Rowe, C. D., White, J. C., & Brodsky, E. E. (2013). Silica gel formation during fault slip: Evidence from the rock record. *Geology*, *41*(9), 1015–1018. https://doi.org/10.1130/g34483.1

Kirkpatrick, J. D., Shervais, K. A. H., & Ronayne, M. J. (2018). Spatial variation in the slip zone thickness of a seismogenic fault. *Geophysical Research Letters*, *45*(15), 7542–7550. https://doi.org/10.1029/2018gl078767

Kirkpatrick, J. D., & Shipton, Z. K. (2009). Geologic evidence for multiple slip weakening mechanisms during seismic slip in crystalline rock. *Journal of Geophysical Research: Solid Earth*, *114*(B12), B12401. https://doi.org/10.1029/2008jb006037

Kohli, A. H., Goldsby, D. L., Hirth, G., & Tullis, T. (2011). Flash weakening of serpentinite at near-seismic slip rates. *Journal of Geophysical Research: Solid Earth*, *116*(B3), B03202. https://doi.org/10.1029/2010jb007833

Lachenbruch, A. H. (1986). *Simple models for the estimation and measurement of frictional heating by an earthquake* (pp. 1–13). U.S. Department of the Interior, Geological Survey.

Lloyd, G. E. (2004). Microstructural evolution in a mylonitic quartz simple shear zone: The significant roles of dauphine twinning and misorientation. *Geological Society, London, Special Publications*, *224*(1), 39–61. https://doi.org/10.1144/gsl.sp.2004.224.01.04

Lloyd, G. E., Farmer, A. B., & Mainprice, D. (1997). Misorientation analysis and the formation and orientation of subgrain and grain boundaries. *Tectonophysics*, *279*(1–4), 55–78. https://doi.org/10.1016/s0040-1951(97)00115-7

Machette, M. N., Personius, S. F., Nelson, A. R., Schwartz, D. P., & Lund, W. R. (1991). The Wasatch fault zone, Utah—Segmentation and history of Holocene earthquakes. *Journal of Structural Geology*, *13*(2), 137–149. https://doi.org/10.1016/0191-8141(91)90062-n

McDermott, R. G., Ault, A. K., & Caine, J. S. (2021). Dating fault damage along the eastern Denali fault zone with hematite (U-Th)/He thermochronometry. *Earth and Planetary Science Letters*, *563*, 116872. https://doi.org/10.1016/j.epsl.2021.116872

McDermott, R. G., Ault, A. K., Evans, J. P., & Reiners, P. W. (2017). Thermochronometric and textural evidence for seismicity via asperity flash heating on exhumed hematite fault mirrors, Wasatch fault zone, UT, USA. *Earth and Planetary Science Letters*, *471*, 85–93. https://doi.org/10.1016/j.epsl.2017.04.020

Mendes, M., & Lagoeiro, L. (2012). Microstructures, crystallographic fabric development and deformation mechanisms in natural hematite aggregates deformed under varied metamorphic conditions. *Journal of Structural Geology*, *40*, 29–43. https://doi.org/10.1016/j.jsg.2012.04.005

Odlum, M. L., Ault, A. K., Channer, M. A., & Calzolari, G. (2022). Seismicity recorded in hematite fault mirrors in the Rio Grande rift. *Geosphere*, *18*(1), 241–260. https://doi.org/10.1130/ges02426.1

Ohl, M., Nzogang, B., Mussi, A., Wallis, D., Drury, M., & Plümper, O. (2021). Crystal-plastic deformation in seismically active carbonate fault rocks. *Journal of Geophysical Research: Solid Earth*, *126*(4), e2020JB020626. https://doi.org/10.1029/2020jb020626

Parry, W. T., & Bruhn, R. L. (1987). Fluid inclusion evidence for minimum 11 km vertical offset on the Wasatch fault, Utah. *Geology*, *15*(1), 67–70. https://doi.org/10.1130/0091-7613(1987)15<67:fiefmk>2.0.co;2

Platt, J. D., Rudnicki, J. W., & Rice, J. R. (2014). Stability and localization of rapid shear in fluid-saturated fault gouge: 2. Localized zone width and strength evolution. *Journal of Geophysical Research: Solid Earth*, *119*(5), 4334–4359. https://doi.org/10.1002/2013jb010711

Pozzi, G., De Paola, N., Holdsworth, R. E., Bowen, L., Nielsen, S. B., & Dempsey, E. D. (2019). Coseismic ultramylonites: An investigation of nanoscale viscous flow and fault weakening during seismic slip. *Earth and Planetary Science Letters*, *516*, 164–175. https://doi.org/10.1016/j.epsl.2019.03.042

Pozzi, G., De Paola, N., Nielsen, S. B., Holdsworth, R. E., & Bowen, L. (2018). A new interpretation for the nature and significance of mirror-like surfaces in experimental carbonate-hosted seismic faults. *Geology*, *46*(7), 583–586. https://doi.org/10.1130/g40197.1

Pozzi, G., De Paola, N., Nielsen, S. B., Holdsworth, R. E., Tesei, T., Thieme, M., & Demouchy, S. (2021). Coseismic fault lubrication by viscous deformation. *Nature Geoscience*, *14*(6), 437–442. https://doi.org/10.1038/s41561-021-00747-8

Précigout, J., & Hirth, G. (2014). B-type olivine fabric induced by grain boundary sliding. *Earth and Planetary Science Letters*, *395*, 231–240. https://doi.org/10.1016/j.epsl.2014.03.052

Prior, D. J., Mariani, E., & Wheeler, J. (2009). EBSD in the Earth sciences: Applications, common practice, and challenges. *Electron Backscatter Diffraction in Materials Science*, 345–360. https://doi.org/10.1007/978-0-387-88136-2_26

Rice, J. R. (2006). Heating and weakening of faults during earthquake slip. *Journal of Geophysical Research: Solid Earth*, *111*(B5). https://doi.org/10.1029/2005jb004006

Robertson, E. C. (1988). *Thermal properties of rocks* (Vol. 88–441, p. 106). U.S. Geological Survey Open-File Reports.

Rosière, C. A., Siemes, H., Quade, H., Brokmeier, H. G., & Jansen, E. M. (2001). Microstructures, textures and deformation mechanisms in hematite. *Journal of Structural Geology*, *23*(9), 1429–1440. https://doi.org/10.1016/s0191-8141(01)00009-8

Rowe, C. D., & Griffith, W. A. (2015). Do faults preserve a record of seismic slip: A second opinion. *Journal of Structural Geology*, *78*, 1–26. https://doi.org/10.1016/j.jsg.2015.06.006

Rowe, C. D., Lamothe, K., Rempe, M., Andrews, M., Mitchell, T. M., Di Toro, G., et al. (2019). Earthquake lubrication and healing explained by amorphous nanosilica. *Nature Communications*, *10*(1), 1–11. https://doi.org/10.1038/s41467-018-08238-y

Sagy, A., Brodsky, E. E., & Axen, G. J. (2007). Evolution of fault-surface roughness with slip. *Geology*, *35*(3), 283–286. https://doi.org/10.1130/g23235a.1

Savage, H. M., & Polissar, P. J. (2019). Biomarker thermal maturity reveals localized temperature rise from paleoseismic slip along the Punchbowl Fault, CA, USA. *Geochemistry, Geophysics, Geosystems*, *20*(7), 3201–3215. https://doi.org/10.1029/2019gc008225

Schmid, S. M., Paterson, M. S., & Boland, J. N. (1980). High-temperature flow and dynamic recrystallization in Carrara marble. *Tectonophysics*, *65*(3–4), 245–280. https://doi.org/10.1016/0040-1951(80)90077-3

Scholz, C. H. (1998). Earthquakes and friction laws. *Nature*, *391*(6662), 37–42. https://doi.org/10.1038/34097

Shervais, K. A., & Kirkpatrick, J. D. (2016). Smoothing and re-roughening processes: The geometric evolution of a single fault zone. *Journal of Structural Geology*, *91*, 130–143. https://doi.org/10.1016/j.jsg.2016.09.004

Sibson, R. H. (1977). Fault rocks and fault mechanisms. *Journal of the Geological Society*, *133*(3), 191–213. https://doi.org/10.1144/gsjgs.133.3.0191

Sibson, R. H. (1992). Fault-valve behavior and the hydrostatic-lithostatic fluid pressure interface. *Earth-Science Reviews*, *32*(1–2), 141–144. https://doi.org/10.1016/0012-8252(92)90019-p

Siemes, H., Klingenberg, B., Rybacki, E., Naumann, M., Schäfer, W., Jansen, E., & Kunze, K. (2008). Glide systems of hematite single crystals in deformation experiments. *Ore Geology Reviews*, *33*(3–4), 255–279. https://doi.org/10.1016/j.oregeorev.2006.03.007

Siemes, H., Klingenberg, B., Rybacki, E., Naumann, M., Schäfer, W., Jansen, E., & Rosiere, C. A. (2003). Texture, microstructure, and strength of hematite ores experimentally deformed in the temperature range 600°C–1100°C and at strain rates between 10^{-4} and 10^{-6} s^{-1}. *Journal of Structural Geology*, *25*(9), 1371–1391. https://doi.org/10.1016/s0191-8141(02)00184-0

Siemes, H., Rybacki, E., Klingenberg, B., & Rosière, C. A. (2011). Development of a recrystallized grain size piezometer for hematite based on high-temperature torsion experiments. *European Journal of Mineralogy*, *23*(3), 293–302. https://doi.org/10.1127/0935-1221/2011/0023-2103

Siemes, H., Rybacki, E., Kunze, K., Klingenberg, B., Naumann, M., Brokmeier, H. G., & Jansen, E. (2010). Development of microstructure and texture of hematite ores deformed to large strain in torsion: Can texture identify the prevailing strength and creep mechanisms during deformation? *Advanced Engineering Materials*, *12*(10), 1003–1007. https://doi.org/10.1002/adem.201000069

Siman-Tov, S., Aharonov, E., Boneh, Y., & Reches, Z. E. (2015). Fault mirrors along carbonate faults: Formation and destruction during shear experiments. *Earth and Planetary Science Letters*, *430*, 367–376. https://doi.org/10.1016/j.epsl.2015.08.031

Smith, S. A., Nielsen, S., & Di Toro, G. (2015). Strain localization and the onset of dynamic weakening in calcite fault gouge. *Earth and Planetary Science Letters*, *413*, 25–36. https://doi.org/10.1016/j.epsl.2014.12.043

Spagnuolo, E., Nielsen, S., Violay, M., & Di Toro, G. (2016). An empirically based steady state friction law and implications for fault stability. *Geophysical Research Letters*, *43*(7), 3263–3271. https://doi.org/10.1002/2016gl067881

Spagnuolo, E., Plümper, O., Violay, M., Cavallo, A., & Di Toro, G. (2015). Fast-moving dislocations trigger flash weakening in carbonate-bearing faults during earthquakes. *Scientific Reports*, *5*(1), 1–11. https://doi.org/10.1038/srep16112

Spray, J. G. (2005). Evidence for melt lubrication during large earthquakes. *Geophysical Research Letters*, *32*(7). https://doi.org/10.1029/2004gl022293

Stipp, M., Stünitz, H., Heilbronner, R., & Schmid, S. M. (2002). Dynamic recrystallization of quartz: Correlation between natural and experimental conditions. *Geological Society, London, Special Publications*, *200*(1), 171–190. https://doi.org/10.1144/gsl.sp.2001.200.01.11

Ujiie, K., Tsutsumi, A., & Kameda, J. (2011). Reproduction of thermal pressurization and fluidization of clay-rich fault gouges by high-velocity friction experiments and implications for seismic slip in natural faults. *Geological Society, London, Special Publications*, *359*(1), 267–285. https://doi.org/10.1144/sp359.15

Ujiie, K., Yamaguchi, H., Sakaguchi, A., & Toh, S. (2007). Pseudotachylytes in an ancient accretionary complex and implications for melt lubrication during subduction zone earthquakes. *Journal of Structural Geology*, *29*(4), 599–613. https://doi.org/10.1016/j.jsg.2006.10.012

Vallina, B., Rodriguez-Blanco, J. D., Brown, A. P., Benning, L. G., & Blanco, J. A. (2014). Enhanced magnetic coercivity of α-Fe_2O_3 obtained from carbonated 2-line ferrihydrite. *Journal of Nanoparticle Research*, *16*(3), 1–13. https://doi.org/10.1007/s11051-014-2322-5

Verberne, B. A., Plümper, O., Matthijs de Winter, D. A., & Spiers, C. J. (2014). Superplastic nanofibrous slip zones control seismogenic fault friction. *Science*, *346*(6215), 1342–1344. https://doi.org/10.1126/science.1259003

Wibberley, C. A., & Shimamoto, T. (2005). Earthquake slip weakening and asperities explained by thermal pressurization. *Nature*, *436*(7051), 689–692. https://doi.org/10.1038/nature03901

Williams, R. T., Rowe, C. D., Okamoto, K., Savage, H. M., & Eves, E. (2021). How fault rocks form and evolve in the shallow San Andreas Fault. *Geochemistry, Geophysics, Geosystems*, *22*(11), e2021GC010092. https://doi.org/10.1029/2021gc010092

Wright, J. K. (1976). The effect of firing conditions on the strength of hematite compacts. *Powder Technology*, *14*(1), 103–113. https://doi.org/10.1016/0032-5910(76)80012-5

Yonkee, W. A., Eleogram, B., Wells, M. L., Stockli, D. F., Kelley, S., & Barber, D. E. (2019). Fault slip and exhumation history of the Willard thrust sheet, Sevier fold-thrust belt, Utah: Relations to wedge propagation, hinterland uplift, and foreland basin sedimentation. *Tectonics*, *38*(8), 2850–2893. https://doi.org/10.1029/2018tc005444